UNIVERSIDAD DE INVESTIGACIÓN DE TECNOLOGÍA EXPERIMENTAL YACHAY

Escuela de Ciencias Físicas y Nanotecnología

**TTTLE: Facile route towards the individualization
of Single-Wall Carbon Nanotubes**

Trabajo de integración curricular presentado como requisito para la obtención
del título de Ingeniera en nanotecnología

Autor:

Berrezueta Palacios Luisa Charlotte

Tutor:

Dr. rer. nat. Chacón Torres Julio C.

Urcuquí, agosto de 2019

SECRETARÍA GENERAL
(Vicerrectorado Académico/Cancillería)
ESCUELA DE CIENCIAS FÍSICAS Y NANOTECNOLOGÍA
CARRERA DE NANOTECNOLOGÍA
ACTA DE DEFENSA No. UITEY-PHY-2019-00016-AD

En la ciudad de San Miguel de Urcuquí, Provincia de Imbabura, a los 23 días del mes de agosto de 2019, a las 14:00 horas, en el Aula Sala Capitular de la Universidad de Investigación de Tecnología Experimental Yachay y ante el Tribunal Calificador, integrado por los docentes:

Presidente Tribunal de Defensa	Dr. REINOSO CARLOS , Ph.D.
Miembro No Tutor	Dr. ZAMORA LEDEZMA , CAMILO , Ph.D.
Tutor	Dr. CHACON TORRES, JULIO CESAR , Ph.D.

Se presenta el(la) señor(ita) estudiante BERREZUETA PALACIOS, LUISA CHARLOTTE, con cédula de identidad No. 0924107832, de la ESCUELA DE CIENCIAS FÍSICAS Y NANOTECNOLOGÍA, de la Carrera de NANOTECNOLOGÍA, aprobada por el Consejo de Educación Superior (CES), mediante Resolución RPC-SO-13-No.156-2015, con el objeto de rendir la sustentación de su trabajo de titulación denominado: Facile route towards the individualization of Single Wall Carbon Nanotubes, previa a la obtención del título de INGENIERO/A EN NANOTECNOLOGÍA.

El citado trabajo de titulación, fue debidamente aprobado por el(los) docente(s):

Tutor	Dr. CHACON TORRES, JULIO CESAR , Ph.D.

Y recibió las observaciones de los otros miembros del Tribunal Calificador, las mismas que han sido incorporadas por el(la) estudiante.

Previamente cumplidos los requisitos legales y reglamentarios, el trabajo de titulación fue sustentado por el(la) estudiante y examinado por los miembros del Tribunal Calificador. Escuchada la sustentación del trabajo de titulación, que integró la exposición de el(la) estudiante sobre el contenido de la misma y las preguntas formuladas por los miembros del Tribunal, se califica la sustentación del trabajo de titulación con las siguientes calificaciones:

Tipo	Docente	Calificación
Presidente Tribunal De Defensa	Dr. REINOSO CARLOS , Ph.D.	9,6
Tutor	Dr. CHACON TORRES, JULIO CESAR , Ph.D.	10,0
Miembro Tribunal De Defensa	Dr. ZAMORA LEDEZMA , CAMILO , Ph.D.	9,7

Lo que da un promedio de: 9.7 (Nueve punto Siete), sobre 10 (diez), equivalente a: APROBADO

Para constancia de lo actuado, firman los miembros del Tribunal Calificador, el/la estudiante y el/la secretario ad-hoc.

BERREZUETA PALACIOS, LUISA CHARLOTTE
Estudiante

Dr. REINOSO CARLOS , Ph.D.
Presidente Tribunal de Defensa

Dr. CHACON TORRES, JULIO CESAR , Ph.D.
Tutor

Dr. ZAMORA LEDEZMA , CAMILO , Ph.D.
Miembro No Tutor

CIFUENTES TAFUR, EVELYN CAROLINA
Secretario Ad-hoc

Hacienda San José s/n y Proyecto Yachay. Urcuquí | Tlf: +593 6 2 999 500 | info@yachaytech.edu.ec

www.yachaytech.edu.ec

Autoría

Yo, LUISA CHARLOTTE BERREZUETA PALACIOS, con cédula de identidad 0924107832, declaro que las ideas, juicios, valoraciones, interpretaciones, consultas bibliográficas, definiciones y conceptualizaciones expuestas en el presente trabajo; así como, los procedimientos y herramientas utilizadas en la investigación, son de absoluta responsabilidad de la autora del trabajo de integración curricular. Así mismo, me acojo a los reglamentos internos de la Universidad de Investigación de Tecnología Experimental Yachay.

Urcuquí, agosto de 2019.

Luisa Charlotte Berrezueta Palacios
CI: 0924107832

Autorización de Publicación

Yo, LUISA CHARLOTTE BERREZUETA PALACIOS, con cédula de identidad 0924107832, cedo a la Universidad de Tecnología Experimental Yachay, los derechos de publicación de la presente obra, sin que deba haber un reconocimiento económico por este concepto. Declaro además que el texto del presente trabajo de titulación no podrá ser cedido a ninguna empresa editorial para su publicación u otros fines, sin contar previamente con la autorización escrita de la Universidad.

Asimismo, autorizo a la Universidad que realice la digitalización y publicación de este trabajo de integración curricular en el repositorio virtual, de conformidad a lo dispuesto en el Art. 144 de la Ley Orgánica de Educación Superior.

Urcuquí, agosto de 2019.

Luisa Charlotte Berrezueta Palacios
CI: 0924107832

Resumen

Los nanotubos de carbono de pared simple, un alótropo de carbono 1D, han llamado la atención de investigadores debido a sus propiedades eléctricas, térmicas, mecánicas y ópticas. La naturaleza de estas propiedades está determinada por su diámetro y quiralidad. A pesar de que se han realizado varios estudios, el uso de los nanotubes SWCNTs sigue siendo limitado debido a la dificultad para ser clasificados. Durante su síntesis, los nanotubos de capa simple crecen y se agrupan en paquetes o "forest" que contienen una mezcla de tubos con diferentes diámetros y estructuras. Para aprovechar sus propiedades intrŋnsecas, se requiere un proceso de separación posterior a su síntesis. Los principales métodos de individualización existentes están basados en el uso of surfactantes o funcionalización en las paredes laterales de los nanotubos lo cual afecta sus propiedades electrónicas. En este trabajo se desarrolló un nuevo método para la individualización de SWCNTs que no requiere el uso de ningún surfactante sino un disolvente polar, tetrahidrofurano (THF). A través de la intercalación con metales alkalinos (i.e. sodio o potasio), un efecto de transferencia de carga *in-situ* es producido en los nanotubos y se induce un desacoplamiento parcial de los nanotubos. Hemos obtenido con éxito un gran número de nanotubos individuales cristalinos confirmados por el Radial Breathing Mode (RBM) en la caracterización por espectroscopía Raman, microscopía electrónica de escaneo (SEM) y microscopía de fuerza atómica (AFM). Adicionalmente, el análisis reveló diferentes grados de funcionalización en los nanotubos dependiendo en el tiempo de sonicación empleado lo cual implica una nueva forma de obtener nanotubos individuales con o sin funcionalización en la superficie.

Palabras clave: SWCNTs, dispersión, exfoliació, nanomateriales, RBMs.

Abstract

Single-walled carbon nanotubes, a 1D carbon allotrope, have drawn significant attention due to their electrical, thermal, mechanical and optical properties. The nature of these properties is determined by their diameter and chirality. Single-walled carbon nanotubes grow in bundles of diverse morphologies. Separation is highly desirable in order to particularly address their electronic properties. The main existing routes to achieve nanotubes individualization are through chemical and physical methods. However, these techniques are based in the use of surfactants or sidewall functionalization which affect their intrinsic electronic properties. In this work I develop a new individualization method for SWCNT that does not require the use of surfactants but a polar solvent instead using dry tetrahydrofuran. This method is based on an in-situ charge transfer effect on carbon nanotubes via intercalation with different alkali metals sodium and potassium followed by a chemical exfoliation process. We have successfully obtained a high number of individualized crystalline Single-walled carbon nanotubes as was confirmed by the Raman Radial-Breathing mode, Atomic Force and Scanning Electron Microscopy. In addition, our analysis revealed that depending on sonication time employed, different degrees of functionalization can be observed in the SWCNT, which excels as a new way to obtain individual carbon nanotubes with or without surface functionalization.

Keywords: SWCNTs, dispersion of CNTs, THF, alkali metals

Acknowledgements

Over the last 5 years since I started this journey, I have encounter many obstacles and challenges during my formation as a Nanotechnology engineer which I had overcome with the support and encouragement of many amazing people. I would like to thank Dr. Julio C. Chacón who has been my advisor for the past year for his advice and mentorship along my journey into becoming a scientific researcher. He provided me with guidance and support along the development of this project.

I would like to acknowledge Yachay Tech university for being the host of my education and the financial support it gave me to be able to attend international conferences, contest and research stays. Also I would like to thank the Institute of Advanced Materials and Processes (ZMP), Friedrich-Alexander-Universitat Erlangen-Nurnberg (FAU), for receiving me into their labs where I conducted the experiments for this research.

Many of my achievements has been accomplished thanks to the support of a great faculty and staff which I had the opportunity to meet and learn from. Therefore I would like to show my gratitude to Alexander Lopez, Juan Lobos, Paola Ayala, Gema Gonzales Sarah Briceño, Evelyn Cifuentes and Jorge Batres for their continued support at different stages of my undergraduate studies.

I want to thank my friends. They made this last years more enjoyable and interesting as we encountered this challenge together. Specially to Lorena Layana, Denise Andrade, David Lajones, Patricio Tinoco, Bernardo Guerrero for putting up with my peculiar mood and being with me anyways.

My family has been a key component during my formation, I would like to thank Rodrigo and Fanny, my grandparents, who are my role models. But there are two special persons I would like to thank the most: Luisa Palacios and Alfonso Berrezueta, my mom and dad. They have encourage me to follow my dreams and never give up. They have support me unconditionally though this long and hard journey.

Contents

List of Figures

List of Tables

List of Papers

[1] C. Berrezueta-Palacios, Claudia Kröckel, L. Layana-Franco, Frank Hauke, Andreas Hirsch, J. C. Chacón-Torres.
Facile route towards the individualization of Single-wall Carbon nanotubes bundles.
Journal of the American Chemical Society (ACS Publications)
(In-preparation 2019)

Introduction

Single-walled carbon nanotubes (SWCNTs) are recognized as an exceptional material that has generated considerable attention among researchers for their interesting physical properties and applications [1,2]. Despite the fact that many studies have been carried out, the use of SWCNTs remains limited because of the difficulty to sorting them. During SWCNTs growth, they get organized in bundles or "ropes" containing a mix of tubes with different structures and properties [3]. To take advantage of their intrinsic properties, a post-synthesis separation process is required.

This work presents a study of a new dispersion method to individualize SWCNTs without the use of any surfactant but a polar organic solvent, tetrahydrofuran (THF). Though the intercalation with alkali metals, a charge transfer effect is produced with SWCNTs and a partial debundling effect is induced. The separation method is completed by further dispersion in THF. The experimental procedure of this research was conducted in the laboratories of the Institute of Advanced Materials and Processes (ZMP) Friedrich-Alexander-Universität Erlangen-Nürnberg (FAU) during a research stay in the Summer of 2018 while the further analysis was performed in Yachay Tech University under the supervision of Dr. Julio Chacón Torres.

The first chapter provides to the reader an introduction to low dimensional carbon-based materials, specifically fundamental concepts about Single-walled carbon nanotubes structural and electronic properties, also the synthesis processes and the state of the art regarding separation and individualization methods. A detailed explanation of the methodology implemented for the individualization process of SWCNTs and the sample preparation is described in Chapter 2. The samples prepared with the procedure described in the previous chapter are analyzed by the characterization techniques described in Chapter 3 called "Introduction to characterization methods". This chapter describes the operating principle of each characterization technique and the conditions under which the samples were measured. Chapter 4 shows the results and the analysis of the data obtained by the characterization of the samples. These results provide information to evaluate the success of the separation and quality itself. Finally, the last chapter is a summary of the results achieved and the outcomes of this research and the most optimal conditions for the separation process.

Chapter 1

Theoretical background

1.1 Carbon-based materials

Carbon has many ways to bond together and form different crystalline or amorphous structures, also called carbon allotropes(see Figure 1.2). To understand carbon-based materials, a review of chemical bonding and electronic configuration of Carbon is necessary. Carbon is the fourth most abundant element in the universe and is considered as the basic element for life. Being part of the group IV, Carbon is the 6th element of the periodic table. A typical Carbon atom is constituted by 6 protons, 6 neutrons, and 6 electrons which occupy the $1s^2, 2s^2, 2p^2$ atomic orbitals in the ground state. The $1s^2$ orbital is occupied by 2 electrons in the inner shell called core electrons and will not have any influence on chemical reactions. There is an energy difference of about 4 eV between the upper $2p$ and the lower $2s$ energy levels, which make that from the four electrons remaining, two occupy the $2s^2$ orbital and two the $2p^2$ orbitals, these are the valence electrons[4]. The binding energy to form chemical bonds is bigger than the orbital energy difference. When an external perturbation is present, the electronic wave function of the valence electrons mixes by exciting one electron from the s^2 orbital and changes its occupation to the third $2p$ atomic orbital. This enhances the formation of covalent bonds with neighboring atoms. $|2s\rangle$, $|2p_x\rangle$, $|2p_y\rangle$, and $|2p_z\rangle$ are the four equivalent quantum-mechanical states as observed in Figure 1.1. sp^n, $n = 1, 2, 3$ hybridization appears by the superposition of a single $2s$ electron with $2p$ electrons[5].

Carbon based structures have three possible hybridizations, sp, sp^2 and sp^3 that will give rise to the formation of different materials such as graphite, diamonds, fullerenes, carbon nanotubes among others. Carbon differs from other elements with the same valence due to the absence of nearby inner orbitals (except for the spherical $1s$) this will ease the hybridizations involving only valence s and p orbitals[6].
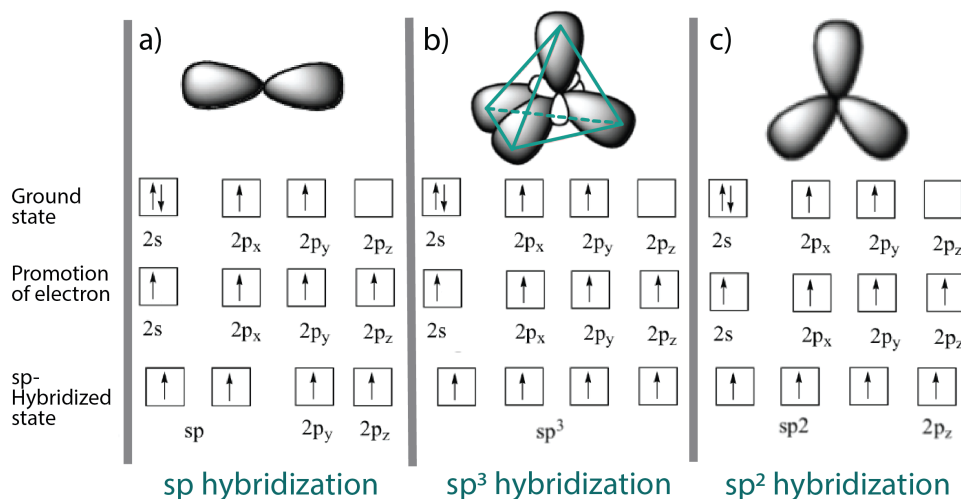
Figure 1.1: Electronic structure of carbon. a) sp^2 hybridization, b) sp^3 hybridization c) sp^2 hybridization.

1.1.1   *sp hybridization*

The *sp* hybridization is formed when the $|2s\rangle$ state mixes with one $|2p_i\rangle$ with $i = x, y$ or z orbital for example $|2p_x\rangle$ and the other two $2p$ states remain unaffected. This superposition of the two-electron orbitals will form two hybridized *sp* orbitals, denoted by $|sp_a\rangle$ and $|sp_b\rangle$. The wavefunction of $|2s\rangle + |2p_x\rangle$ and $|2s\rangle - |2p_x\rangle|$ will elongate positively and negatively along the x-direction respectively (see Figure1.1 a). When a neighboring atom approaches in direction of x-axis, $|sp_a\rangle$ has higher binding energy compared to $|2p_x\rangle$ function itself. The overlapping of one hybridized $|sp_a\rangle$ orbital of two carbon atoms will form a covalent bond called σ bond. The two unhybridized orbitals $|2p\rangle$ from carbon will form two π bonds with the ones from the other carbon atom which are weaker than σ bond. The linear molecule acetylene HC≡CH, which plays an important role in the context of organic chemistry[6,7].

1.1.2   *sp³ hybridization*

When the 2s orbital is mixed with the three *p* orbitals, sp^3 hybridization is produced. Four hybrid orbitals are formed $|sp_a^3\rangle$, $|sp_b^3\rangle$, $|sp_c^3\rangle$, $|sp_d^3\rangle$ with elongated wavefunctions in the following directions (1,1,1), (-1,-1,1), (-1,1,-1), (1,-1,1)[6]. The orbitals form a 109.5° angle with a tetrahedral assembly (see Figure1.1b). In the corners of this 3D assembly, a covalent bond will form with another carbon atom, where a strong binding strength is produced. The sp^3 hybridization gives rise to the formation of diamonds, one of the hardest materials known[8] (see Figure1.2 b).

1.1.3 *sp² hybridization*

The formation of sp^2 hybridization occurs when the $2s$ orbital is combined with two $2p$ orbitals, probably $|sp_x\rangle$ and $|sp_y\rangle$ states. This produces three quantum states $|sp_a^2\rangle$, $|sp_b^2\rangle$, $|sp_c^2\rangle$ that will form a planar hybridization along x and y plane. Thus σ bonds will be formed in each hybrid orbital at a 120° angle (see Figure 1.1 c). The unaffected orbital $|sp_z\rangle$ will form a π bond perpendicular to the in plane sp^2 hybrid orbitals[6].

For instance, graphene is a carbon-based allotrope derived by a sp^2 hybridization. In this structure, each carbon atom is bonded to three other carbon atoms by a σ bond resulting in a hexagonal planar lattice[9](see Figure1.2 c). Graphene is known as the basic constituent of graphitic systems. When several layers of graphene are stacked one to another by weak van der Waals interactions (weaker in comparison to interplanar covalent bonds) graphite is obtained (see Figure 1.2 d)[10]. Other examples of graphitic allotropes are Carbon nanotubes and fullerenes. Fullerenes are a $0D$ carbon allotrope (see Figure 1.2 e) discovered by Kroto in 1985[11] (Nobel prize in Chemistry 1996 to Robert F. Curl Jr., Sir Harold W. Kroto, and Richard E. Smalley). The C_{60} fullerene, also called buckyball, is a soccer ball-shaped molecule. It can be thought as a graphene structure where pentagons are placed instead of hexagons to bend into a sphere[11]. Fullerenes can have metallic or semiconductor properties and their mechanical properties resemble the ones of diamond[12]. Another graphitic allotrope is carbon nanotubes (CNTs) (see Figure1.2 f). This $1D$ structure can be thought of as one or several graphene sheets rolled up into a concentric seamless tube[6]. They show a high length/diameter ratio[13]. Depending on the number of rolled up sheets, nanotubes can be classified into single-wall or multi-wall nanotubes with diameters between 5-20 nm, separated by a distance of 0.34 nm[14].
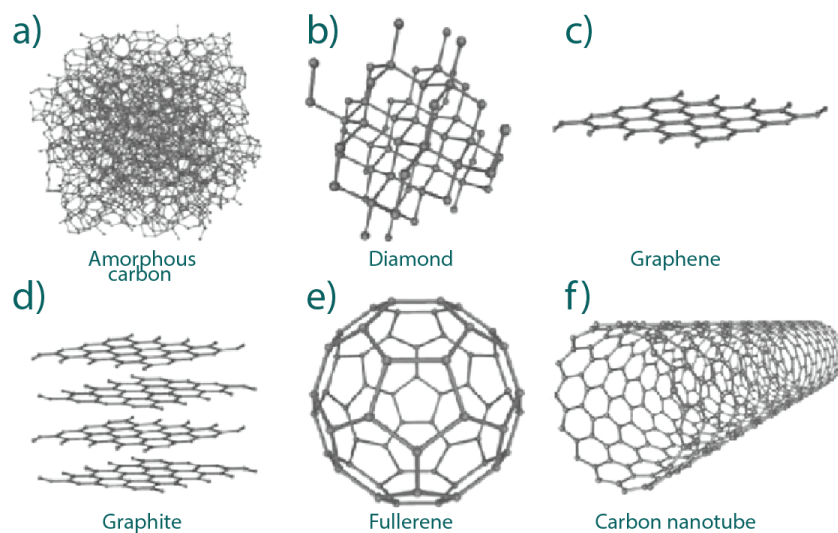
Figure 1.2: Some of the structures of various carbon allotropes. a) Amorphous carbon. b) Diamond. c) Graphite. d) Fullerene. e) CNT. f) Graphene. Adapted from[15]

As described previously in this section, even though carbon is the atomic component, depending on its hybridization, it will form several materials with completely different properties. Carbon allotropes, particularly, single walled carbon nanotubes upon other materials show excellent properties that will be described in the next section.

1.2   Single-walled carbon nanotubes (SWCNTs)

Notwithstanding, the first observation of carbon nanotubes dates back to 1952 by two Russian scientists Radushkevich and Lukyanovich[16], the interest in carbon filaments did not reached a big impact until 1991 when Sumio Iijima, in his paper "Helical microtubules of graphitic carbon" provided a description of the preparation of needle-like tubes with a hexagonal lattice arranged in a helical fashion around the needle axis[14]; opening a brand new field for material sciences. Big interest and enthusiasm lie in the fascinating properties that SWCNTs exhibits. From their first studies to most recent research, over 36800 papers have been published regarding nanotubes research with an increasing number of papers each year *. Single-walled carbon nanotubes show mechanical[17,18], electrical[19], and thermal[20] properties unheard of in any other material. They are extremely stiff, displaying Young's modulus close to 1 TPa, and are among the world's strongest materials, with strength between 50 and 100 GPa[17]. Nanotubes are predicted to have a very large thermal conductivity of up to 6 000 W/m*K[21–23]. These physical properties combined with their relative ease of preparation, makes them a suitable model system for one-dimensional physics and a good candidate material for possible applications in nanodevice engineering and technological applications[3,24].

The structure of carbon nanotubes exhibits a spiral conformation, which is called the chirality of the nanotube. This large variety of possible helical geometries will provide a wide array of structures (chirality and diameters) that will define the nanotube physical and electronic properties[6].

1.3   Structure of SWCNT

In this section we will introduce the basic concepts and parameters that determine the characteristics and properties as well as the structure of carbon nanotubes. There exist a relationship between SWCNTs and graphene that will allow the deduction and understanding of SWCNT's structure and properties. To understand their structure, each single-wall carbon nanotube needs to be thought of as a conformal map of a two-dimensional lattice of a graphene sheet projected onto the surface of a cylinder[25]. One important aspect when analyzing the structure of carbon nanotubes is their symmetry. When discussing the physical properties of carbon nanotubes, we use their characteristic high aspect ratio to neglect the tubular caps at the ends of the tube.

---

*From Institute of Scientific Information; general search with keywords "nanotube"

The crystal lattice structure of graphene is made out of a two-dimensional rhombus that contains two carbon atoms enclosed per unit cell (see Figure1.3.) $\vec{a_1}$ and $\vec{a_2}$ are the primitive unit vectors positioned to form a $60°$ angle between them and the length of the lattice constant is the same as for 2D graphite ($a = 2.46$Å) and is given by $|\vec{a_1}|=|\vec{a_2}|= \sqrt{3}a_0$ where a_0 is the distance between two neighboring carbons atoms C-C (1.42Å).

$$\vec{a_1} = \frac{a}{2}(\sqrt{3}\hat{x} + \hat{y}) \quad \text{and} \quad \vec{a_2} = \frac{a}{2}(-\sqrt{3}\hat{x} + \hat{y}) \tag{1.1}$$
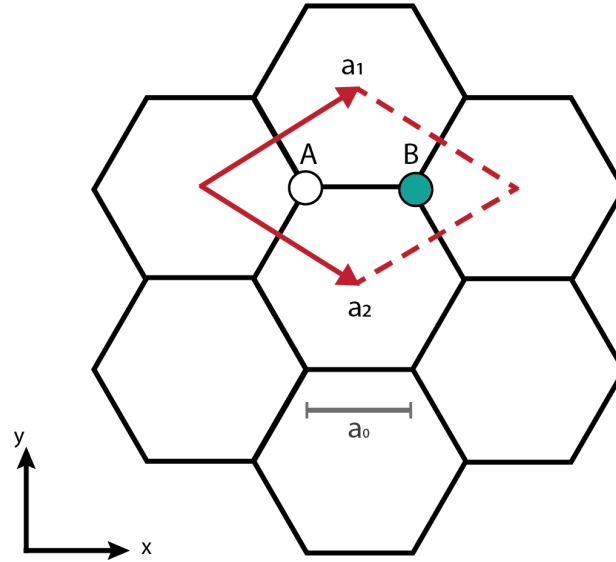
Figure 1.3: The honeycomb lattice of graphene. The unit cell defined by vectors $\vec{a_1}$ and $\vec{a_2}$ containing the two atoms belonging to sublattices A (white) and B (blue) is highlighted in light blue.

SWCNT can be characterized by only one vector describing the path along the circumference of the nanotube. Thus each real lattice vector of the two-dimensional hexagonal lattice (the Bravais lattice for the honeycomb) defines a different way of rolling up the sheet into a nanotube. Such lattice vector is called chiral or roll-up vector C (see Figure1.4 a). There are two parameters that control the structure of a nanotube, its diameter and its chiral angle or twist along the tube axis. Both are specified completely by C, which is generally defined in terms of the two basis lattice vectors $\vec{a_1}$ and $\vec{a_2}$ and a pair of integer indexes (n, m)[25,26].

$$C = n\vec{a_1} + m\vec{a_2} \tag{1.2}$$

The diameter of a tube is directly related to the chiral vector C as it connects two equivalent positions along the lattice which lie on top of each other when rolled up to form the SWCNT. Therefore, the absolute value of C provides
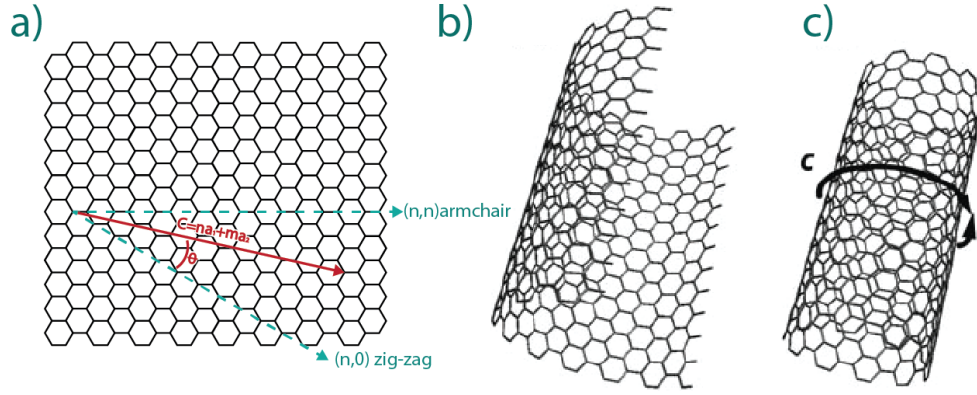
Figure 1.4: Carbon nanotubes structure. A strip is cut out of graphene (a) and then rolled up (b) to form a seamless cylinder (c). Adapted from [28]

the circumference of the tube and its diameter is given by [27]:

$$d = \frac{|c|}{\pi} = \frac{a_0}{\pi} \sqrt{n^2 + nm + m^2} \tag{1.3}$$

Based on the graphene's lattice symmetry, the arrangement of the graphene hexagons on the wall of the tube will be specified by the angle between the lattice vector $\vec{a_1}$ and the chiral vector C defines the second characteristic parameter, the chiral angle (θ) [29].

$$\cos(\theta) = \frac{C \cdot \vec{a_1}}{|C| \cdot |\vec{a_1}|} = \frac{an + m}{2 \sqrt{n^2 + nm + m^2}} \tag{1.4}$$

The allowed values for the chiral angle vary between $0° \leq \theta \leq 30°$; all other ranges of θ are equivalent to this interval because of the hexagonal symmetry of graphene. This angle will specify the primary symmetry classification of a carbon nanotube as either being achiral (symmorphic) or chiral (non-symmorphic). This characteristic is determined by the shape of the cross-sectional ring also seen as the edge of a C_{60} molecule bisected at the equator [6,30].

An achiral carbon nanotube exist when the mirror image of a carbon nanotube has an identical structure to the original one (particular high symmetry) the edge of a C_{60} molecule bisected at the equator [6]. There exist two types of achiral nanotubes; armchair and zigzag nanotubes. Zigzag nanotubes alignment follows the structure of a C_{60} molecule bisected normal to a 3-fold axis, forming a zigzag chain at the edge. For these series of carbon nanotubes, the chiral angle is $\theta = 0°$ $(n, 0)$. If the C_{60} molecule is bisected normal to a five-fold axis, an armchair tube is formed. These structures have $\theta = 30°$ and the edge of their unit cell looks like a row of armchairs when viewed from above, hence the name. All other existing SWCNTs with $(n = arbitrary, m \neq n \neq 0)$ are called chiral [30]. They exhibit a spiral asymmetry and a mirror image that cannot be superimposed on to the original one [31]. The chiral vector not only determines the tube diameter and chiral angle but other parameters as the length and the number of carbon

atoms in the unit cell. There is a dependency between the electronic properties of a SWCNT and its structural indices (n,m)[30].

1.4 Electronic structure of SWCNTs

The electronic structure of a single wall carbon nanotube can be described from a graphene sheet[32]. The calculated electronic structure of nanotubes depend on their diameter and chirality. (n,m) indices will denote metallic and semiconducting behavior for the nanotubes. For nanotubes, periodic boundary conditions upon the wave function that can be applied along its chiral vector while the wave vector associated with the translational vector remains continuous for a nanotube length. This is due to the fact that nanotubes can be conceived as a seamless rolled sheet of graphene.

1.4.1 Density of States

A one-dimensional system with energy bands can be extended into a 2D reciprocal space from a graphene sheet approximated by a parabolic shape (see Figure 1.5 a), that will be represented as a set of equidistant cutting lines near the K point. The one-dimensionality of the CNTs gives rise to a local maximum at each cutting line producing a discrete set of singularities, known as van Hove singularities (vHS) which have relevant importance for the Raman spectra of nanotubes (see Figure 1.5 b)[32]. E_0 corresponds to a vHS in the Density of states (DOS), $n(E) = \Delta N/\Delta E$ the number of available states ΔN in a given energy interval ΔE with $\Delta E \to 0$. The magnitude of the DOS is larger at certain energetic levels with a sharp threshold and a decaying tail that will appear at each sub-band edge[32]. $E^{(v)}$ corresponds to the electronic sub-bands at the valence band and $E^{(c)}$ for the conduction bands.
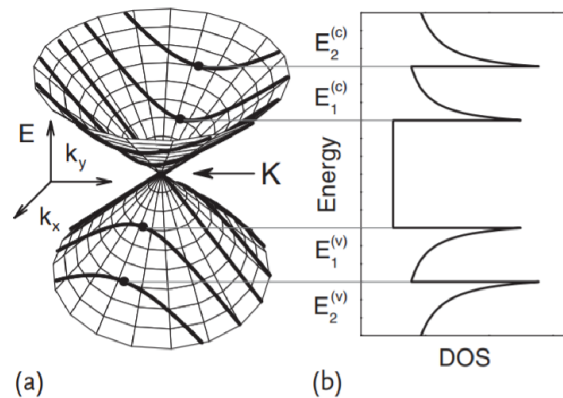
Figure 1.5: 1D density of states of a carbon nanotube

High values of the DOS allow the observation of physical phenomena of the 1D material, for example, the electrical properties of the nanotubes (metallic or semiconducting). Metallic carbon nanotubes exhibit valence and conduction bands touching. The allowed cutting lines will cross the Fermi level at the K point of the first Brillouin zone. Nanotubes that have a zero energy gap DOS between valence and conduction bands up to the first van Hove singularity, will be semiconducting and their gap will depend inversely on the carbon nanotube diameter[6]. Carbon nanotubes have well-defined electronic DOS, their energy levels will be different for each (n,m) indices[33]. A Raman signal from a carbon nanotube will be observed when the laser excitation energy is equal to the energy separation between vHS in the valence and conduction bands, but they will be restricted to the selection rules for optically allowed electronic transitions[32].

1.5   Synthesis Methods of SWCNTs

In this section I will introduce the main synthesis methods to produce carbon nanotubes that have been developed through the pass of years. Each process has its advantages and disadvantages[6]. The first method known for producing CNTs dates back to their first discovery by Iijima, where the procedure of mass production of C_{60} fullerenes was slightly adapted to grown graphitic carbon needles on the negative end of the carbon electrode used in the DC arc-discharge evaporation of carbon[14].
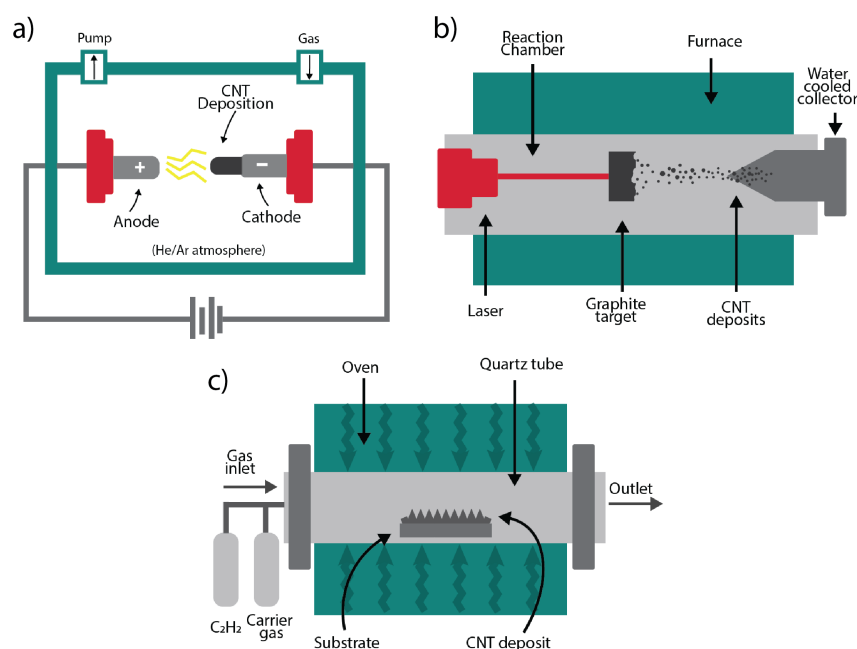
Figure 1.6: Schematic representation of methods used for carbon nanotubes synthesis a) Laser ablation b) Arc discharge c) Chemical vapor deposition

1.5.1   Arc-Discharge

In a more detailed way, the arc-discharge procedure consists in placing 2 rods graphitic electrodes ranging from ~5 to 20 millimeters in diameter, one of them can contain traces of particles from a transition metal of iron or cobalt that work as a catalyst leading to the formation of single-walled carbon nanotubes at a distance of around 1 mm[14]. During this procedure, both electrodes are enclosed in a sealed vacuum chamber at ~500 torr under an atmosphere of argon or helium. By placing a voltage of 20-25 volts across the electrodes and a DC current of 50-120 amps across the electrodes, a temperature of up to 3000°C is reached. This temperature is high enough for the sublimation of carbon atoms out of the solid electrode material into a plasma, and a carbon "soot" is deposited on the negative electrode as observed in Figure 1.6 a)[34,35]. The majority of the SWCNT produced is bound together by Van der Waals interactions and form bundles of nanotubes. By an optimization process maximal yield of about 50 wt% in the soot containing SWCNT can be achieved using a carbon anode containing 1 at.% of yttrium and 4.2 at.% of nickel as catalyst. The range of a nanotube diameter produced by the arc-discharge method lies between 0.75 and 1.2 nm[24].

1.5.2   Laser Ablation

A few years later, in 1996, Richard Smalley et al. perfected laser ablation technique that yielded up to 70% of carbon material transformed into single-walled carbon nanotubes[3]. The principles and mechanisms of this system are similar to the arc discharge technique. Its difference lies in the energy source, that in this case is provided by a neodymium-yttrium-aluminum-garnet laser which is placed at one end of a long quartz tube and a water cooled copper collector at the other end, in a furnace heated around 1200°C[36] (see Figure 1.6 b).

These two high temperature synthesis techniques (arc-discharge and laser ablation) will produce byproducts during the growth of the carbon nanotubes as described above. The isolation and cleaning of the carbon nanotubes from these byproducts is a complex task. For instance centrifuging and sonication techniques break apart the nanotubes reducing their length[37]. For that reason, new synthesis methods that produce longer lengths were needed and not long time after low temperature chemical vapor deposition (CVD) techniques (<800°C) appeared[38].

1.5.3   Chemical Vapor Deposition

The CVD method required the use of a gaseous carbon sources such as methane or acetylene which are mixed with noble gases or hydrogen. At temperatures of about 1000°C by the use of suitable catalyst materials ie. Fe, Co, Ni in the reaction chamber, nanotubes are formed[38] as seen in Figure 1.6 c). The process can be modified by use of plasma irradiation, which leads to lower defect rates in the formed carbon nanotubes[39]. Chemical vapor deposition has become one of the most widely used growth techniques because they offer a high degree of control on the morphological parameters such as orientation, alignment, nanotube length, diameter, density and scalability of the CNTs[40,41]. It is possible to grow nanotubes on well-defined places with specific patterned substrates or produce an individual tube that bridges two catalytic particles[42,43]. The great disadvantage of CVD relies in the lower quality

that this material presents and a continuous study in this field towards the development in terms of better quality, purity, yield, and length is required including on the theoretical side which will give a better understanding of the processes.

High Pressure Carbon monoxide (HiPco®) process is a CVD method developed in 1999 for the synthesis of single-walled CNTs[44]. It is described by the catalytic production of single-walled CNTs in a continuous-flow gas-phase using carbon monoxide as the carbon feedstock and $Fe(CO)_5$ (iron pentacarbonyl) serves as catalyst precursor. The products of $Fe(CO)_5$ thermal decomposition react to produce iron clusters in gas phase that will serve as a nuclei for the SWCNTs to nucleate and grow through solid carbon produced by the disproportionation of CO. These particles will be responsible for the formation of the hexagonal carbon lattice of the tube[44]. The temperature used ranges from 800 - 1200°C to grow SWCNTs. The $CO/Fe(CO)_5$ flow mixes through the heated reactor resulted in black deposits on the walls of the quartz tube outside the furnace. These deposits consisted of SWCNTs and iron particles apparently overcoated with carbon[45].The architecture of the reaction chamber has an influence on the yield while the pressure roughly controls the diameter distribution of the nanotubes. In this way the HiPco® process can deliver thin SWCNTs of diameters between 0.7-1.2nm without amorphous carbon over-coating them that can interfere with most of the interesting properties of nanotubes. However, the problem with the synthesis of carbon nanotubes through the introduced methods is when synthesized, SWCNTs self-organize into rope-like crystallites also known as bundles containing a mixture of semiconducting (2/3) and metallic (1/3) SWCNTs[45]. A post-synthesis separation process and/or purification methods are needed along the synthesis of CNTs.

1.6   Dispersion of SWCNTs in aqueous solvents

The manipulation and processing of nanotubes are one of the current challenges that researchers have encounter in nanotubes application[46]. Dispersion in aqueous solutions is a required process for enhancing their intrinsic properties by breaking up the bundles. The main issue of this process, is the inherent insolubility of the SWCNTs in neither water or common solvents (polar or non-polar)[47]. This is due to the Van der Waals interactions among the high number of nanotubes. These interactions will cause the rearrangement of individual CNTs into entangled bundles. Many studies have been performed towards the optimization and development of processes for an effective separation[48]. The dispersion of CNTs differs from other nanomaterials mainly due to their large surface area produced by their small diameter with a high aspect ratio (>1000). Surfactants are one of the main approaches for dispersion as it has been demonstrated that they can enhance their suspendability in solution[49]. The $\pi - \pi$ stacking (van der Waals interactions) and hydrophobic interactions are the two main factors that affect this dispersion.

Nanotubes dispersion methods can be classified by their physical and chemical treatment. Common physical dispersion methods include ultrasonic, high-speed shearing, grinding, ball mill and using supercritical fluids[50]. Ultrasonic and high-speed shearing are reliable methods that allow the dispersion of CNTs into liquids that normally will not disperse in water, polymers, ethanol and even oil. Ultrasonic processes break the agglomerate structures by transferring energy into the liquids and can be used for high concentrated samples. There are two ways to perform

this technique, by an ultrasonic bath or an ultrasonic tip (sonicator)[51]. A higher ultrasonication time will determine the quality of the dispersion of the CNTs by incrementing the dispersion and disentangling of CNTs[52]. Ball mill on the other hand, grinds the pristine material into a fine powder which provides a uniform length distribution and better dispersion in contact with the solvent[51].

Chemical treatments are categorized by the use of surfactants, functionalization or treated the CNTs with aggressive agents such as strong acids. These methods generate an improvement of the adhesion and wettability of the carbon nanotubes by modifying their surface energy[53]. Chemical treatments reduce the tendency to agglomerate in an aqueous phase by acid oxidation and free radical reaction[54]. Surfactants being a dispersing agent accelerate the dispersion effect of CNTs by being absorbed by the nanotube surface and create high local shear acting as spacers between the nanotubes[55,56]. Functionalization and the use of surfactant techniques modifies the surface of the nanotubes, altering their properties and improving the interaction with the solution to be dispersed in. In this case, functional groups are covalently added to generate stronger interactions with the dispersing agent. The introduction of another component or the modification of a side wall will produce an alteration to the pristine intrinsic properties such as mechanical, electrical or optical[57,58]. Whether they are physical or chemical treated, CNTs require a post-synthesis separation method in order to enhance their full potential.

1.7 Intercalation Compounds

Intercalation compounds are defined as complex materials produced by a reversible insertion process in which ions or molecules guest species are accepted by a host lattice without altering its structural features[59]. The main characteristic of intercalations is that intercalation compounds require a reversibility property that allows the return to the initial state through electrical thermal or chemical actions[60]. The interest in intercalation reactions is the degree of perturbation of their chemical, electronic and optical properties. There exist two types of interactions within the host and the accepted molecules: electropositive or organic and inorganic molecules[61]. Electropositive elements will determine the ionization and exhibit high mobility in the structure for example elements like alkali metals able to set weak bonds with the host structure. Low dimensionality solids arranged in slabs and fibers are good candidates to be used as host structures due to high anisotropy in their chemical bonding where the intraplanar binding forces are large in comparison with the interplanar binding forces, usually linked by the van de Waals type such as carbon-based materials, transition metal oxides, aluminum oxide host[59].

1.7.1 Graphite Intercalation compounds

One of the most studied interaction systems is graphite intercalation compounds (GIC) because they display excellent physical and chemical properties comparable to those of pristine graphite[62]. Graphite is a mineral layered structure material made of several graphene layers. GIC structure is formed by foreign species that are inserted between these graphene layers in the interplanar interstitial site and expanding the interplanar space, but the layered structure of the graphite lattice is retained[63]. The properties of GIC (physical and chemical) are governed by the bonding

environment between the carbon atoms and the intercalant and by the intercalant itself. Intercalant species can be alkali metal, metal oxides, metal chlorides, bromides, fluorides, oxyhalides, acidic oxides or Lewis acids, among others [64]. Depending on the character of the bonding, graphite intercalation compounds can be classified into two groups: covalent (homopolar) or partially ionic (polar). Homopolar groups are formed when the carbon in the layer planes changes its hybridization from sp^2 to sp^3 creating conjugated double bonds within the carbon plane. The second group corresponds to partially ionic bonding, meaning that the degree of ionicity in compounds of this group may be very low and therefore the molecular identity is kept making the type of bonding more complicated [63].

Chapter 2

Motivation

As discussed in the previous chapter, nanotubes do not grow individually but in bundles of mixed morphologies and chiralities. Further dispersion is required to take advantage of their intrinsic properties. Current separation methods (described before) increase the solubility of CNTs in different solvents. The problem in CNTs dispersion lies in the fact that these methods can damage or alter the structure and properties of the nanotubes. When the treatment is too vigorous or exposed for a long interval, the nanotube can get fragmented and shorter in length (physical treatments). On the other hand, chemical modification processes create a functionalization that results in defects in the CNT lattice. Therefore, the design and development of an optimal, clean and precise individualization process for SWCNT that does not require modify their intrinsic properties is one of the major challenges in current nanotechnology[56]. Several studies have been performed on many solvents in order to solubilize pristine nanotubes. Dimethylformamide (DMF), N-methylpyrrolidone (NMP), hexamethylphosphoramide (HMPA) and Tetrahydrofuran (THF), Lewis bases, have been investigated as good candidates for the dispersion of nanotubes aggregates due to their high electron pair donicity and low hydrogen-bonding. These features have demonstrated their ability to create a stable dispersion[65]. However, generally these methods result in a partial exfoliation of the big bundles into smaller size bundles but not fully individualized tubes. Additionally, the electron doping is not enough to keep a stable solution since in a long time-scale, and after few days, the dispersed samples reaggregate.

In this project I focus on the development of a new separation method for SWCNT that does not require the use of surfactants. This methodology is based in a charge transfer effect on carbon nanotubes via intercalation with alkali metals followed by a chemical exfoliation process. The separated SWCNT will be obtained through a tip sonication dispersion process in THF. We aim for the obtention of a high yield of individualized crystalline SWCNT. The rate of success in this process will be evaluated by means of Raman spectroscopy and AFM analysis. Through several experiments based on this principle, the most optimal process for individualization is acquired and through a Raman analysis of the spectra, an assignment of the obtained chiralities is performed. This thesis will introduce a new field in SWCNTs research as a model system for one-dimensional physics that will stand for future optimal nanoelectronics.

Chapter 3

Methodology

This chapter describes the experimental procedure followed to achieve the successful individualization of SWCNTs without the use of surfactants but a polar solvent instead. This methodology is based on an in-situ charge transfer effect on carbon nanotubes by a reduction reaction with alkali metals. We performed an intercalation of pristine SWCNTs powder with sodium (Na) and potassium (K) that produced reduced carbon nanotubes. This negatively charged nanotubes also called nanotubides[66] will result in an electrostatic repulsion between themselves inducing a partial debundling effect that will lead to ramified SWCNTs. Finally, high-quality individualization is obtained via a chemical exfoliation process induced by the dispersion of CNTs in dry tetrahydrofuran (THF), a polar aprotic solvent, using a tip sonication process as shown in Figure 3.1.
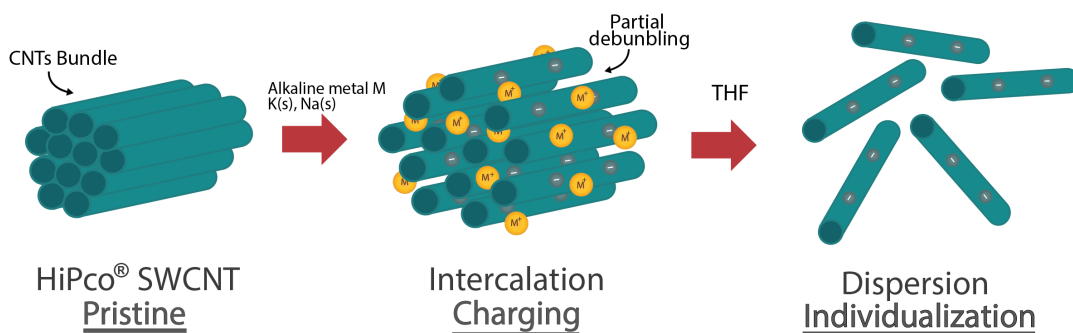
Figure 3.1: Scheme of the individualization process implemented applied to CNTs bundles through the intercalation with alkali metals and further dispersion in THF.

The compounds of graphite intercalated with alkali metals, are among the most studied of graphite materials[67]. In their pure form, alkali metals are shiny, soft and highly reactive compounds. These metals react readily with air and

moisture[68]. Upon exposure to air at room temperature, alkali metals will ignite spontaneously to form caustic metal oxides. Meanwhile, in contact with water, alkali metals react vigorously and produce heat, flammable hydrogen gas and the corresponding metal hydroxide. The heat produced by this reaction may spontaneously ignite the hydrogen or the metal itself, resulting in a fire or an explosion[69]. The use of potassium, sodium or other alkali metals requires handling with air-free techniques such as an inert atmosphere to conduct in the experiment. Therefore, this study was run inside a glove box under an argon atmosphere with (<0.1 ppm oxygen, 0.1 ppm H_2O) and reactives such as solvents and CNTs were submitted to a drying process before use.

3.1   Drying Solvents

Any liquid that has been exposed to ambient conditions contains appreciable amounts of dissolved gasses and impurities that should be eliminated before their use, by conducting a proper purification and degassing process[70]. The presence of dissolved gases like oxygen or carbon dioxide can alter chemical reactions, interfere with spectroscopic measurements and produce different results[71]. The term degassing refers to the process by which dissolved gases like oxygen and other gaseous atmospheric contaminants are removed from a liquid[71]. There are many techniques available to degases liquids. For example: heating, ultrasonic agitation, chemical removal of gases, substitution with inert gas by bubbling and freeze-pump-thaw cycling[70]. THF solvent to be used in the separation process of the CNTs was prepared by three purification processes: absorbents-Molecular sieves, free-pum thaw and distillation.
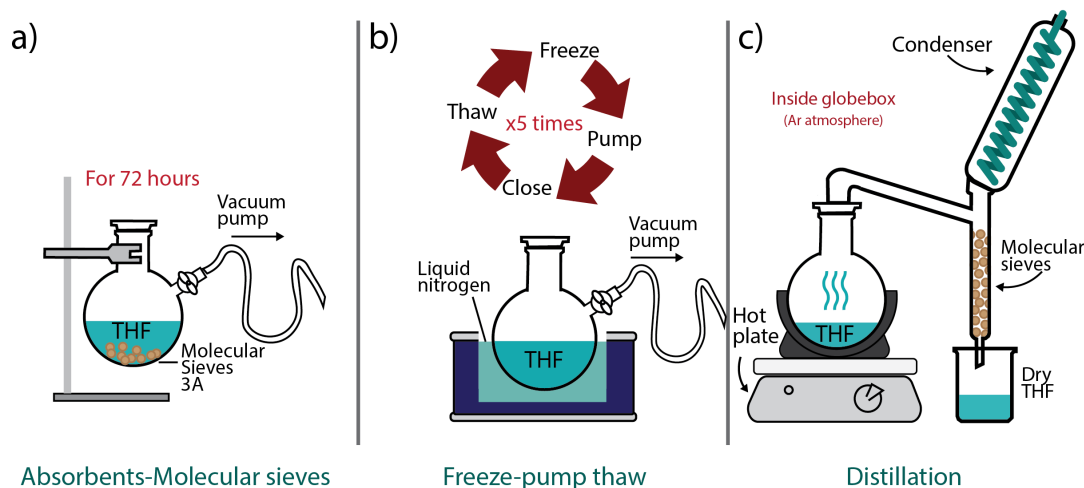
Figure 3.2: Schematic representation of the methods used to dry the THF solvent before use a) Molecular sieves, b) Freeze-pump thaw, c) Distillation

3.1.1   Absorbents-Molecular sieves

One of the ways to remove water from solvents is by absorbents. Molecular sieves and alumina are the most common absorbents used to attain very low moisture levels and the absorbent has to be activated prior to be used. Molecular sieves are synthetic porous crystalline aluminosilicates which have been engineered to have the ability to selectively discriminate on the basis of molecular size[72]. 3Å molecular sieves (do not adsorb molecules whose diameters are larger than 3Å) were used. The purification of the solvent to be used for the separation process was carried out continuously by pouring the solvent with the molecular sieves during 72 hours under vacuum (see Figure 3.2 a).

3.1.2   Freeze-pump thaw

If the amount of compounds is small or if the material is thermally sensitive, as the case of THF, freeze-pump (thaw) is the method of choice under a reduced pressure, and by using a high vacuum/inert gas double manifold[73], as it is described in[74]. In this project, we placed the solvent to be degassed (THF) in a glass flask with a stopcock or valve that is suitable for evacuation. After extracting the solvent from the molecular sieves, THF was initially frozen in the cold bath using liquid nitrogen (before freezing, the flask environment must be free of oxygen to prevent the condensation of liquid oxygen upon freezing). Vacuum is then applied and the headspace above evacuated. After the stopcock is closed, the solvent is thawed allowing the releases of dissolved gaseous species that emerge as gas bubbles. The freezing process was then repeated up to 5 cycles to decrease the percentage of dissolved gasses to the minimum (2.4ppm in 0.2782g) (see Figure 3.2 b).

The solubility of a gas in a liquid follows the pressure dependence phenomenon described by Henry's law (equation 3.1), which states that the amount of dissolved gas (C_{aq}) is directly proportional (k) to its partial pressure (P_{gas}) in the gaseous state above the liquid under constant temperature, volume and pressure[75].

$$C_{aq} = kP_{gas} \qquad (3.1)$$

Introduction of a vacuum above the sample will reduce the partial pressure of the gas above the liquid and hence reduce the solubility of dissolved gases within the solvent making the liquid-gas phase equilibrium be re-established[76].

3.1.3   Distillation

For the removal of other impurities present in the sample, distillation under an inert atmosphere is employed. After pump-freeze purification process, THF was introduced into the glovebox. Solvents were distilled from a distillation flask containing either a metallic metal, benzophenone or calcium hydrate. For distillation of THF, a small amount of sodium potassium alloy was used. The sample then gets heated until boiling under a vigorous stirring. Expelled gasses travel from the flask to the distillation column and condensate in the water-cooled condenser. The distillate is

then collected at the top of the column in the distillation trap and decantates through a molecular sieves column and they are stored in a previously dried flask (0.8 ppm in 2.26408 g) (see Figure 3.2 c). The process used followed[71].

3.2 Drying CNTs

As with solvents, solid compounds require also a degassing process to eliminate H_2O moisture and oxygen. The SWCNTs sample used in this study was synthesized by the well-known CVD HiPco process provided by Unidym. The diameter range of the nanotubes is between ~0.8-1.2 nm. In order to use the pristine nanotubes for the separation process, a drying of the nanotubes powder needs to be done. The sample was placed inside a Schlenk flask and then vacuum was applied. With a heating gun, the flask was uniformly heated up for 5 min and let cool down, this will extract the molecule of oxygen from the nanotubes and the walls of the flask. When the container gets hand warm, apply argon to the system. Due to difference in molecular weight, oxygen, which is lighter, will go up and get extracted when vacuum is applied. The process was repeated 5 times (see Figure 3.3).
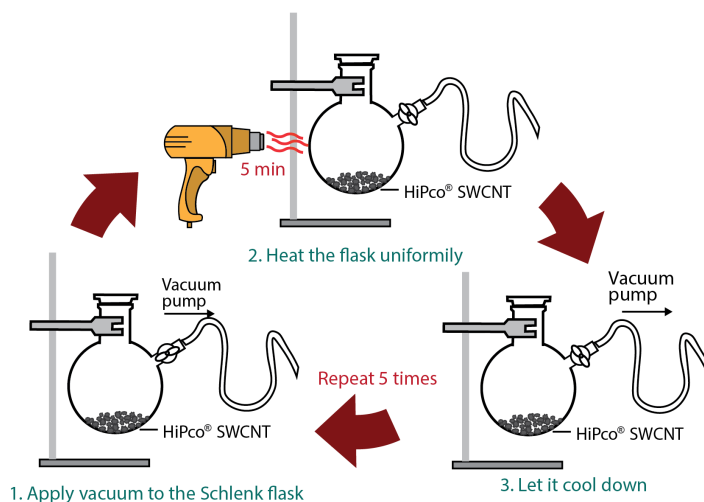
Figure 3.3: Schematic representation of the drying process of CNTs.

3.2.1 SWCNTs intercalation compounds

The same principle as in graphite alkali metals is used for SWCNTs individualization. Graphite-alkali metals are a binary system that belongs to the class of "ionic" intercalation compounds. This is a n-type intercalation where alkali metals are used as a donor guest to dope graphite. The interaction of the guest with the host in reduced graphite intercalants is done by a charge transfer process, expanding the van der Waals gap between the layers[63,77]. Due to the crystalline structure of SWCNTs bundles, the interstitial space and the internal cavity of nanotubes are good

candidates for alkali-metal adsorption[78]. As with alkali atoms in GIC, when intercalated, a fraction of electronic charge from the alkali metal is transferred to the nanotubes. Nanotubes get negatively charged and is expected that repulsion between them will induce a partial exfoliation process from bundles of SWCNTs[79].

In this project, two alkali metals were used in the separation process, sodium and potassium. Three different intercalation compounds were produced: KC_8, KC_{24}, and NaC_8. Intercalation was conducted inside an Ar glovebox. Each sample was prepared by melting the alkali metal over previously dried SWCNTs powder. Sodium and potassium are soft solids, with low melting points[80], they were cut with a knife, melted and then mixed with the nanotubes inside a glass vial at 200°C for 72 hours under Ar atmosphere with stirring each 20 minutes for the first hour.

Chapter 4

Introduction to characterization methods

4.1 Raman Spectroscopy Technique

In this section, the fundamental concepts of Raman spectroscopy characterization are introduced. The section starts with a description of the electromagnetic scattering process which is one of the basic concepts of spectroscopy and then into different scattering processes.

4.1.1 Light Scattering

The interaction of light with matter can occur in three different ways. Incident photons can be absorbed (see Figure 4.1 a), scattered or they may pass through without any interaction (reflected) (see Figure 4.1 b). Light scattering can be conceived as the redirection of light that occurs when an incident electromagnetic (EM) wave (for instance monochromatic radiation) come upon a solid, gas or liquid material (see Figure 4.1 c)[81] As the incident EM wave interacts with matter (material to be analyzed), a periodic perturbation on the electron cloud within the constituent molecules is generated. The perturbation will have the same frequency (ω_o) as the electric field of the incident wave[82]. In this way, the charge will separate periodically within the molecules, this effect is called induced dipole moment[83]. A new source of EM radiation is generated from the oscillating induced dipole moment and manifested as scattered light. The scattering process can be elastic or inelastic depending on the difference between the spectrum of the incident light with respect to the scattered light[84]. Most of the radiation scattered by the irradiation of a monochromator is emitted at the same wavelength as that of the incoming laser radiation so-called elastic scattering. Inelastic scattering process relates to the small additional light scattered at different wavelengths from the incident light. Raman scattering is an example of inelastic scattering that is used for molecular identification by providing chemical and structural information[85].
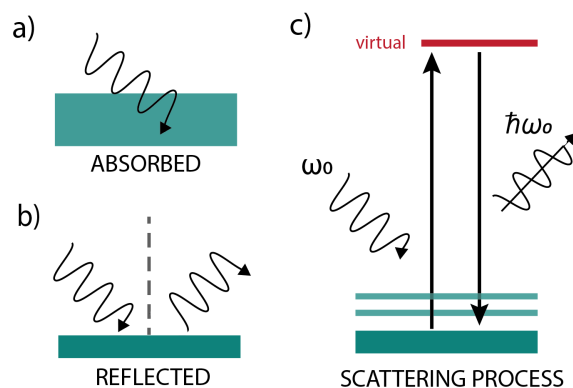
Figure 4.1: Scheme of the interaction between light and matter: a) Light absorbed by matter, b) Reflection of incident light wave, c) Light scattering by an induced wavelength.

4.1.2 Raman Spectroscopy

Different scattering frequencies can be explained by the classical description. The contents of this section is a restatement based in the equations and descriptions found in ref([82]). A dipole moment (P) is induced by the time-dependent electric field of a monochromatic incident light of frequency ω_0 over a molecule. The dipole moment strength is given by:

$$P = \alpha \overline{E} \tag{4.1}$$

where α is the polarizability, a material property dependent on molecular structures and atom-atom length. α is generally expressed as a function of the inner atomic distances and will directly depend on the molecular frequency oscillation ($\omega_i\ [Hz]$), incident EM ($\omega_0 = c/\lambda$) and the Electric field $\overline{E} = E_o \cos{(2\pi\omega_0 t)}$. Substituting the electric field into equation 4.1 yields the time-dependent induced dipole moment,

$$P = \alpha E_o \cos{(2\pi\omega_0 t)} \tag{4.2}$$

vibrational modes of individual atoms when forming a molecular bond are quantized similarly to electronic energies as $E_{vib} = (j + \frac{1}{2})h\omega_{vib}$. The physical vibrational displacement dQ of the atoms about their equilibrium position due to vibrational modes ω_{vib}.

$$\mathrm{d}Q = Q_0 \cos{(2_{vib}t)} \tag{4.3}$$

where Q_0 is the maximum displacement about the equilibrium position. The polarizability can be approximated by a Taylor expansion because the maximun physical displacement for an atomic molecule is small (about 10% of the bond length).

$$\alpha = \alpha_0 + \frac{\partial \alpha}{\partial q}\mathrm{d}Q \tag{4.4}$$

where α_0 is the polarization of the molecule at equilibrium position. When substituting the vibrational displacement from equation 4.3 into equation 4.4 the polarizability is expressed as

$$\alpha = \alpha_0 + \frac{\partial \alpha}{\partial q} Q_0 \cos\left(2_{vib}t\right) \tag{4.5}$$

with this new expression of the polarizability, the dipole moment defined in equation 4.1 can be expressed as

$$P = \alpha E_o \cos\left(2\pi\omega_0 t\right) + \frac{\partial \alpha}{\partial Q} Q_0 E_0 \cos\left(2\pi\omega_0 t\right) \cos(2\pi\omega_{vib}t) \tag{4.6}$$

using a trigonometry identity, the previous relation can be rearranged as

$$P = \alpha E_o \cos\left(2\pi\omega_0 t\right) + \left(\frac{\partial \alpha}{\partial Q}\frac{Q_0 E_0}{2}\right)\{\cos\left[2\pi(\omega_0 - \omega_{vib})t\right] + \cos\left[2\pi(\omega_0 + \omega_{vib})t\right]\} \tag{4.7}$$

From equation 4.7, at three distinct dipole frequencies are created ω_0, $\omega_0 - \omega_{vib}$ and $\omega_0 + \omega_{vib}$. The scattering radiation is emitted at these three same frequencies. Vibrational spectroscopy detects the change in energy of those that cause nuclear motion. A photon from the incident EM wave excites an electron from the ground state into a short live state, called "virtual" energy state. This state is not stable and the photon is quickly re-radiated. ω_0 frequency is formed when only the electron cloud distortion is involved, the photons in the light scattered do not gain or lose energy along the interaction with the sample. Therefore it exits with the same wavelength as the incident hence is
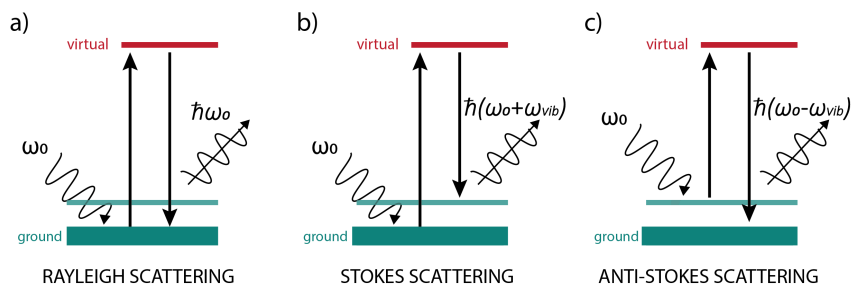
Figure 4.2: Conceptual scheme of the light scattering processes: a) Rayleigh scattering, b) Stokes scattering c) Anti-stokes scattering.

elastic scattering also known as Rayleigh scattering process (see Figure 4.2 a). Inelastic scattering takes place if nuclear motion is induced. The energy will be transferred in one of the following two ways: from the incident photon to the molecule or from the molecule to the scattered photon resulting in an energy difference between the incident and the scattered photon by one vibrational unit. therefore, $\omega_0 - \omega_{vib}$ and $\omega_0 + \omega_{vib}$ frequencies will show a shift to higher or lower frequencies. The scattered light of these two cases is known as Raman scattering. It is inherently a weak process where only one in every $10^6 - 10^8$ scattered photons is Raman scattered. Down-shifted frequency (longer frequency) the molecule absorbs energy and its promoted from ground state (*m*) to a higher vibrational state (*n*). This effect is called Stokes Scattering (see Figure 4.2 b). When a molecule is at an excited state (*n*) (e.g due to thermal energy) scattering to the ground state transferring energy to the scattered photon and the frequency will experiment an up-shift (shorter wavelength) referred to as anti-Stokes scattering (see Figure 4.2 c)[81,86].

4.1.3   Vibrational Modes

Raman spectroscopy is an important tool regarding the analysis and characterization of carbon based materials. For SWCNTs, Raman Spectroscopy provide information about crystallite size, the introduction of chemical impurities, mass density, the optical energy gap, elastic constants, doping, defects and other crystal disorder, nanotube diameter, among other characteristics [87]. A Raman spectra is a plot of the intensities of scattered portion of incident light versus the shifts in the frequency between the incident and the scattered light [88]. There are many features that can be identified with specific Raman scattering processes that contribute to each feature of SWCNTs such as the radial breathing mode (RBM), the G-band, the dispersive disorder induced D-band and its second-order related harmonic G'-band [89].

The G^+ peak corresponds to atomic displacements along the tube axis and G^- for modes with atomic displacement along the circumferential direction [90]. The G^+ does not show significant difference in frequency or width depending on their electronic type [91]. The difference is observable in the G^- feature. The spectrum taken shows a very broad a G^- feature is seen, that can be described by a BreitWignerFano (BWF) lineshape. This asymmetric and broad lineshape is characteristic for metallic nanotubes [92] compared to semiconducting tubes, where the G^- follows a Lorentzian lineshape. This broadening is related to the presence of free electrons in nanotubes with metallic character [91,93].

Through the intensity of the RBM feature, the electronic type of the nanotubes can also be distinguished. Very close but intense RBM features are observed in the region from $\sim 150 cm^{-1}$ to $\sim 350\, cm^{-1}$ as observed in Figure5.1a). The frequency of an RBM peak (ω_{RBM}) is highly dependent on the diameter (d) of the nanotubes and are related by the following expression [94]:

$$\omega_{RBM} = \frac{A}{d} + B \tag{4.8}$$

Where A and B are constant coefficients. Several A and B combinations have been reported in literature [95]. These values depends on several factors like growth methods, diameter distribution, the dispersion environment, the substrate among others [29]. As previously explained in Chapter 1 section 3, the diameter is related to the (n,m) index and therefore its electronic structure. The frequencies observed will determine the structural assignments of the tubes. The most intense peaks in the RBM region of the pristine spectrum are seen at around 244, 261 and 269cm^{-1}. This RBM spectrum agrees with the peaks from a study performed on HiPco® bundles with a green laser (1.41 eV) [96]. The high number of frequencies observed in this region, corresponds to a diameter distribution of different SWCNTs in resonance at this excitation laser which suggest a large number of chiralities present in the pristine sample.

4.2   Scanning Electron Microscopy

One important non-destructive characterization technique used to observe, analyze, and explain the morphology of nanostructures or other materials is scanning electron microscopy (SEM). SEM is an important technique which allows the observation and characterization of heterogeneous organic and inorganic materials and surfaces on such a local scale by producing a largely magnified image by using electrons instead of light to form an image [97]. It

irradiates a focused electron beam, which may be static or swept in across the surface or area of the specimen to be examined. The resulting interaction of the electrons from the beam source with the sample, produce various signals used to obtain information regarding surface topography and composition of the sample[98].

The types of signals obtained by SEM produce secondary electrons, backscattered electrons, Auger electrons, characteristic x-rays, and photons of various other energies[99]. The two most interesting signals in SEM are the secondary electrons (SE) and backscattered electrons (BSE) due to their variation in the signal received as a result of differences in surface topography as the electron beam is swept across the specimen[100]. The electron microscope was developed when the wavelength became the limiting factor in light microscopes. The distance at which two points apart can be distinguished is called resolution. Though the use of lenses or an assembly of lenses the human eye resolution (0.2 mm) can be increased, this is the case for optical microscopes. Although the development of better lenses has continued through the years, the limitation of the resolving power of the microscopy was not limited by the lens quality but for the wavelength of the light source. White light has wavelengths from 400 to 700 nanometers (nm). Electrons have much shorter wavelengths, enabling better resolution[99]. The SE emission is confined to a volume near the beam impact area this allows the obtention of a relatively high-resolution[98].

4.2.1 SEM Working Principle

The stream of electrons is produced by an electron gun, depending on the electron gun, these primary electrons are accelerated through a voltage difference between the anode and the cathode with a range between 0.1 keV to 50 keV. The accelerated electrons carry significant amounts of kinetic energy. These accelerated primary electrons are directed by the condensing lens system and scanning coil to be incident on the sample with the smallest beam cross-section at the gun so that an electron probe of diameter 1-10 nm carrying an electron-probe current of 10^{-9}-510^{-12} A is formed[98]. Due to the electron-sample interactions, the electrons are decelerated and the energy is dissipated into a variety of signals mentioned above. SE and BSE are collected on a photomultiplier tube, which convert the electrons into an electric signal that will be amplified to obtain an image[101].

4.2.2 Electron-specimen interaction

When the accelerated electrons hit the specimen, the interaction can result in elastic or inelastic scattering. The elastic events affect the trajectory of the electron beam without significantly altering the energy and inelastic events leading to a transfer of energy to sample producing secondary electrons, Auger electrons, and x-rays[98]. For BSE, a significant fraction of the incident beam, undergo sufficient scattering events to completely reverse and escape from the specimen and provide information regarding specimen composition, mass thickness and crystallography. BSE show a dependence on the atomic number (increasing with atomic number), energy dependence (there is a small dependence of BS with the beam current) and tilt dependence (tilting angle at which the beam strickes the sample will decrease the interaction volume)[101]. Low energy SE are created when weakly bond valence or conduction electrons are ejected. Due to their low kinetic energy, they will suffer rapid energy loss with the distance traveled. As the electron beam moves deeper into the sample, the escape probability will decrease exponentially[102]. SE also show

dependence on the atomic number due to the number of outer shell electrons and atomic radius. Tilting the stage of the sample will increase the electron coefficient. Secondary electrons are most valuable for showing morphology and topography on samples.

4.2.3 Key components of SEM

There are several factors that will influence on the final resolution of the SEM. One of them is the amount of current of the final electron beam that strikes against the sample, this will determine the signal magnitude. Another important factor that will determine the best scanning possible resolution is the size of the final probe. The electron optical system is designed to obtain the maximum possible current in the smallest possible electron probe[98]. These factors can be varied by the components and the design of the electron optical column. Next, it is presented the main components of SEM and their working principle to obtain an image[99].

Electron guns

The source of electrons necessary for SEM to operate is produced by an electron gun. Electron guns provide a steady source of electrons manifested as an electron beam. There are many types of electron guns: tungsten cathode, lanthanum hexaboride cathode, but the two main types of electron guns are thermionic and field emission guns. Thermionic emission of electrons is achieved when high thermal energy is applied to a filament giving to a percentage of the electrons sufficient energy to overcome the work function and steam away the electrons from the source. In field emission guns, the cathode in the form of a rod with a very sharp point is held at a negative potential relative to the anode. By generating a strong electric field at the tip, the potential barrier becomes narrow, allowing the electrons to tunnel and leave the cathode without any thermal energy. with an effective brightness higher than thermionic sources. Electron guns are located either at the very top or at the very bottom of an SEM and the fired beam of electrons don't go naturally directly into the sample, they need to get directed by the other components of the SEM[98].

Lenses

SEM uses electromagnetic lenses. As with optical lenses, SEM lenses are used to obtain clearer and detailed images[99]. The electron beam is focused and controlled by the electromagnetic field interaction of the lens and the moving electrons. The condenser and objective lens system are used to demagnify the image by directing to converge or diverge the e beam. The condenser lens system will determine the beam current meanwhile objective lens determines the final spot size[98].

Sample chamber

The sample to be analyzed is placed inside a chamber. The quality of the image can be decreased by small perturbations like vibrations. Therefore, the sample must be still during the measurement. The sample chamber including the sample stage must be insulated from vibrations. For conventional SEM to work properly, the specimens

to be observed need to be at high vacuum. When the electron beam emitted by the electron gun travels through the optical system, if the systems are not under vacuum conditions, particles from the atmosphere will interfere and cause attenuation or distortion of the surface of the specimen[98].

Detectors

Detectors are devices implemented to detect the different interactions of the electron beam with the sample by converting the radiation that leaves the specimen into an electrical signal. Important parameters to take into account are the relative angle to the specimen surface, the range of solid angle over which the detector accepts a signal and the conversion efficiency. Different types of detectors will receive different signals. For instance, for secondary electrons, Everhart-Thornley detector.[103], a type of collector-scintillator-photomultiplier system is used. meanwhile, for BSE common detectors types are scintillator or of semiconductors.

4.3 Atomic Force Microscopy

The branch of microscopy that image surfaces by scanning a specimen through a physical probe is called Scanning Probe Microscopy (SPM)[104]. Higher resolution without damage is obtained by scanning the interaction over the specimen at each point of the area between the probe and the specimen as a function of the position[105]. SPM can measure physical properties like surface conductivity, static charge, distribution, magnetic field, and elastic moduli though the interactions based on physical principles such as atomic force, capacitance friction or magnetic fields[106]. Atomic Force Microscopy (AFM) is a very high-resolution type of scanning probe microscopy. The invention of AFM arises from the scanning tunneling microscope (STM) that allowed the imaging of metal and semiconducting surfaces at an atomic resolution. In 1982, Binning and co-workers invented the STM[107]. The limitation of STM (only works with conduction materials) led to the development of a new technique to study non-conductive materials, AFM was invented[108]. Over the years, many improvements have been done in AFM like the invention of the dynamic, taping and non-contact taping mode[109]. This technique is used for the study of the topography and properties of a sample (specific material or biological samples) with a resolution ranging from microns to sub nanometers[105,108]. Its importance encompasses different fields of science like material science, molecular biology, fundamental surface science, and roughness analysis[105] because through this technique a larger surface area per mass of material can be analyzed and a bigger amount of information regarding their mechanical properties can be extracted. It consists of a mechanical microscope composed by the scanning unit, the cantilever with a sharp tip (see Figure 4.3), the optical detection system, and the electronic feedback. This technique is based on the detection forces between the probe tip at one end of a spring-like cantilever and the surface of the sample. The tip-sample interaction in close proximity to each other will produce either attractive or repulsive forces. These forces give information to rise a three-dimensional image based on the sample topography controlled in all axes by means of a piezoelectrical scanning unit which consists of a vertical and a lateral positioner.

4.3.1   Configuration and working principle of the AFM

A schematic image of the AFM components is present in Figure 4.3. The cantilever acts as a force sensor. Due to the interaction forces between the samples and the tip, the cantilever will deflect while raster-scanning the tip over the sample surface. Typical cantilever dimensions are in the order of hundreds of microns (100 to 400 μm long). The appropriate size of the tip will affect the amount of information acquired from the surface features and atomic resolutions. To have a small sensitivity to the force, the spring constant (k) needs to be chosen in the range of 0.01-100 nm[110]. There are many types of cantilevers and their shape will depend on the kind of measurement that will be conducted. The most common feature to be analyzed is the sample topography, but there exist other properties like variations in local stiffness[111], friction force[112] and lateral stiffness[113] that can be measured.
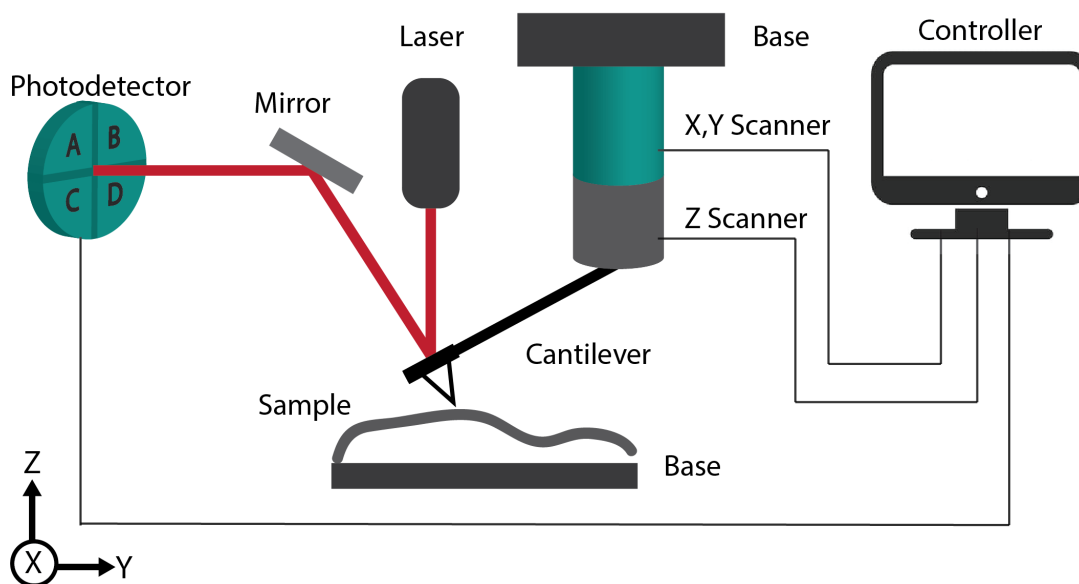
Figure 4.3: Configuration of the components in an atomic force microscope.

The piezoelectric XYZ is a scanner implemented to control the movement of the probe along the sample substrate in both in the lateral (X, Y) and vertical (Z) directions and provides an image in three dimensions. Sample topography will be obtained by a lateral scanning of the cantilever deflections and the plane friction forces will cause a twist around its longitudinal axis. The flexural and torsional bending of the cantilever is measured by an optical detection system. The reflection of an incident laser beam over the back of the surfce of the cantilever. Any deflection will cause changes in the direction of the reflected beam which is registered by a high-resolution deflection detector. A deflection detector is a position-sensitive detector (PSD) that can measure small or large variations. The PSD consists of a photodetector segmented into four quadrants. The difference between optical powers from upper vs lower quadrants or left vs right quadrants in the photodetector will provide the fluxural and torsional signals.

4.3.2 AFM Working Modes

Depending on the separation distance between the sample and the tip, different forces will be involved. The most common force associated with atomic force microscopy is a weak interatomic force called the van der Waals force[105]. The dependence of the Van der Waals force upon the distance between the tip and the sample is shown in Figure 4.4. The operation modes of AFM can be discussed in terms of the applied force regimes or in terms of the force sensing technique employed[114]. The AFM has two main general modes: a) the static mode (also known as contact mode) and b) the dynamic mode (the non-contact mode and the tapping mode).

In each mode, there is a dominant interaction force that rules over. When two atoms are separated by distances smaller than 10 nm, such that the long-range attractive force between the atoms of the tip and the sample is perceptible. These attractive forces are observed in the non-contact mode and are called dynamic modes because the cantilever oscillation is close to its resonance frequency[114]. When the separation is smaller than 1 Å, there is an overlap of the electron cloud and the ionic interactions which cause a repulsive force. The repulsive forces are used for contact mode. The tip of the cantilever scans across the sample while a feedback loop maintains constant cantilever deflection and force[114].
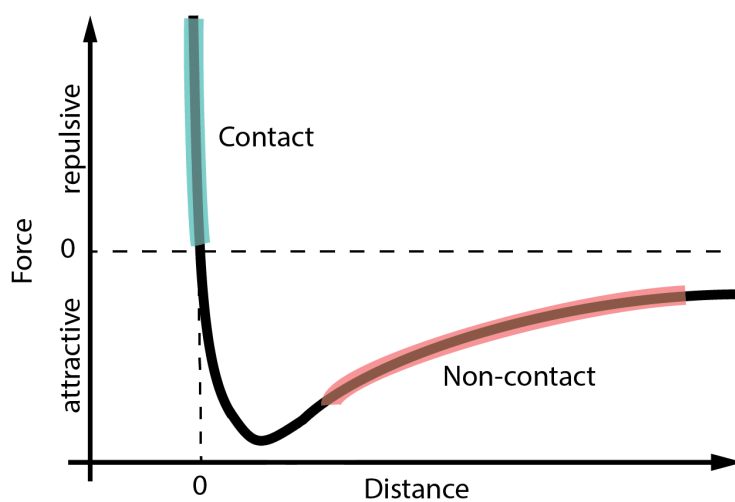
Figure 4.4: Interatomic force variation with respect to the distance between AFM tip and sample.

Contact Mode

Contact mode is the simplest working mode. Also known as static mode, the sharp probe tip is adjusted until it makes a continuous soft physical contact with the sample. The probe tip is attached to one end of the cantilever with a low spring constant. When the cantilever pushes the tip against the sample, the interactive forces are in the repulsive region therefore, the cantilever bends rather than forcing the tip samples closer to the sample atoms (see

Figure 4.4 blue shade region). The cantilever deflection is measured as the scanner traces the tip across the sample. The cantilever is moved in the vertical direction, during the lateral scanning, to maintain the tip-sample force as constant as possible[109]. The cantilever is considered a spring were k is the constant force. By Hook's law, the corresponding force is proportional to the deflection. The contact mode has the disadvantage that, both the sample and the tip may experience damages due to lateral forces[110].

Non-contact Mode

In this mode, the tip of the cantilever is brought close to the sample at a constant distance. The tip vibrates near the surface near the resonance frequency, where *k* is the spring constants of the cantilever and *m* is the mass of the spring-like cantilever. The system mechanically excites the oscillations on which the cantilever is mounted (typically from 100 to 400 kHz) with an amplitude of a few tens to hundreds of angstroms[106]. The cantilever must be stiffer than in the contact mode, this allows the cantilever to have a small bending and a high force sensitivity to detect changes in the resonant frequency or vibrations amplitude as the tip comes near the sample surface due to the varying shape topography. The interacting forces are attractive. These forces are very weak which is good because the samples do not suffer degradation effects that sometimes can be observed with contact AFM due to close contact (see Figure 4.4 red shade region). This is preferable for the imaging soft samples.

Tapping Mode

Tapping mode can be thought of as a mix between contact and non-contact modes where the tip is brought to oscillate intermittently at a resonance frequency unlike in the non-contact mode where there is no contact at all[115]. In this way, the lateral and normal forces exerted on the tip on the sample are diminished. When the tip of scans and interacts with the surface, changes in oscillation amplitude or phase are detected. This operation mode can be described as driven damped harmonic oscillator plus the interaction between the tip and the sample. Interactive forces will be in both attractive and repulsive regime. If the amplitude is small (1 nm) the tip-sample interacting force will be in the attractive regimes. At a higher value such as 100 nm the tip-sample interacting force can reach the repulsive regime[109].

4.4   Experimental Setup

The characterization of the samples prepared in this study were performed in the Institute of Advanced Materials and Processes (ZMP), Friedrich-Alexander-Universitat Erlangen-Nurnberg (FAU). In order to analyze the samples, the Raman measurements of the SWCNTs individualization were performed with Horiba Scientific - LabRAM Aramis Raman spectrometer using a laser of 532 nm. SEM images were produced with a FEI-HELIOS NanoLab 600i FIB equipment with 10 kV as the applied voltage. The AFM images were obtained with the Bruker ICON Cover Assy REVC Dimensionequip ment.

Chapter 5

Results & Discussion

This chapter is the core of this thesis project since it describes and shows the results obtained at each step of the process conducted towards the optimization of a new separation method to individualize SWCNTs through a non-destructive process that does not require the use of surfactants. As described in chapter 3, the general process consists in achieving the separation of the nanotubes through intercalation with an alkali metal to induce a partial debundling and finally disperse them in THF by tip sonication. To achieve a successful separation, many parameters like concentration, sonication time, precipitation time, among others were varied and sorted in three different sets. At each set, different processes and parameters were tested. After analysis, the process with better results was optimized and implemented into the next set. Hence, the results are shown chronologically as they were studied and optimized. The results presented in this section were characterized by non-destructive techniques AFM, Raman spectroscopy and SEM.

The first section describes the pristine (initial) material an identifies the characteristics peaks of SWCNTs in a Raman spectrum. Next section shows how good is the dispersion of pristine SWCNTs on the organic solvent used, THF. Intercalation was performed with two alkali metals sodium and potassium at the following concentrations 1:8 (*stage I*) for Na and K (NaC$_8$, KC$_8$) and 1:24 (*stage II*) for potassium(KC$_{24}$). By Raman spectroscopy, we proved the obtention of a successful intercalation. Section 4 shows the first set of samples prepared with three initial proposed processes. From a Raman and AFM analysis, I was able to discard KC$_8$ intercalation compound from the process, as well as the process that includes centrifugation as they show a bad dispersion and contamination, respectively. The best process of **SET I** was used as a baseline for **SET II**, where 7 processes were studied under a lower dispersion concentration. AFM profiles allow a qualitative analysis of the separation obtained from which a comparative analysis between the intercalation concentration and the alkali metal samples is performed to obtain the best conditions for the separation method. Once these conditions are determined, **SET III** is a straightforward process of NaC$_8$ and KC$_{24}$ at two phases. Further analysis is presented by comparing a fitting of the peaks from the RBM region obtained by Raman spectroscopy with literature to provide an assignment of possible chiralities of the nanotubes at the final step of the separation process.
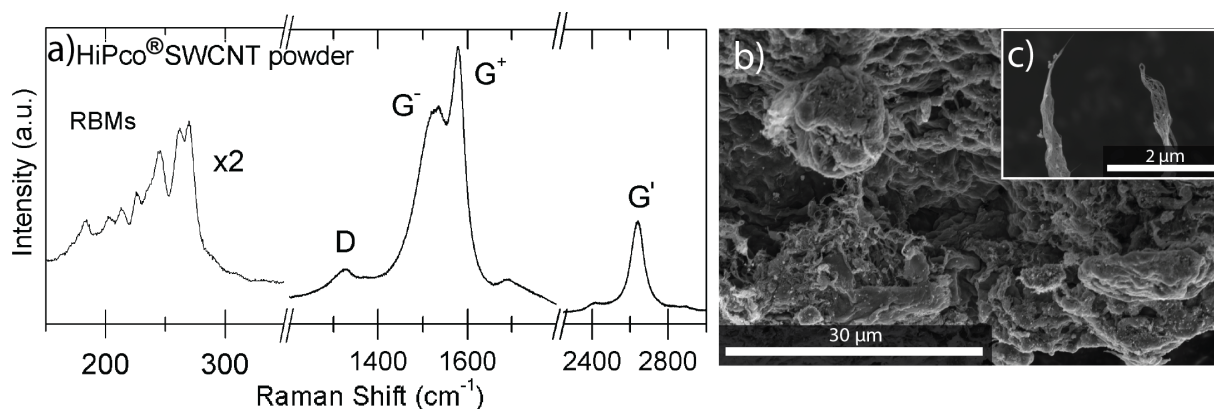
5.1 Pristine HiPco® SWCNT

Figure 5.1: a) Raman spectra (under 532 nm excitation) of HiPco® SWCNT, b)Scanning electron microscopy of pristine HiPco® SWCNT powder.

The starting material is raw HiPco® Single-wall carbon nanotubes acquire from Unidym. The bulk material comes in the form of bundles produced by high-pressure carbon monoxide method. The sample was not treated to any purification process after production but it was dried before being introduced into the glove box as described in section 2 from Chapter 3. The nanotubes have a purity of < 35% of residual Fe Catalyst in weight[68]. The pristine morphology displayed with SEM image in Figure 5.1 b) agrees with literature[68]. The dry bulk SWNCTs powder sample was attached to the aluminum sample stub using conducting carbon tape and measured by SEM with a beam voltage of 5kV. In the SEM image one can observe the fibrous powder with a rough surface. There are fibers like structures corresponding to bundles of SWCNTs which are better observed at Figure 1.5 c), in a close up image of the sample. Other particles are also present in the SEM image which could be assigned to carbonaceous impurities. Over the sample, it is observed an entanglement of the nanotubes into bundles and none individual nanotube can by identified. This agrees with the morphology of this material presented in literature[68]. Additional information regarding this samples was obtained by the Raman response spectrum of the tubes from the bulk material. This and further Raman spectrum measured over a silicon dioxide wafer. A peak that comes from the Si substrate is featured at 520 cm^{-1}, this is used for calibration of the spectra.

Figure 5.1 a) shows the Raman spectrum from the HiPco® pristine sample irradiated with a 532 nm (2.33eV) excitation laser from ~ $150cm^{-1}$ to ~ $3000cm^{-1}$. The samples analyzed showed the three dominant Raman features: the Radial Breathing Mode (RBM) at low frequencies, the tangential (G-band) multifeature and the G'-band at higher frequencies. The figure 5.1 a) shows a double peak structure of the G-line at around 1530 cm^{-1} (G^-) and 1577 cm^{-1} (G^+) that corresponds to tangential vibrations along the nanotube walls[116]. Tangential modes can be

used to distinguish between semiconducting and metallic SWCNTs. The spectrum taken shows a very broad a G^- feature is seen, that can be described as BreitWignerFano (BWF) lineshape. This asymmetric and broad lineshape is characteristic for metallic nanotubes[92]. This broadening is related to the presence of free electrons in nanotubes with metallic character[91,93]. Another characteristic SWCNT Raman feature is present in the spectrum analyzed, the defect related D-band at $1330cm^{-1}$ and the G'-band $2700cm^{-1}$[6]. They arise from one- and two-phonon, second-order Raman scattering processes[117]. The intensity ratio between this the D-band compared to the G-band (D/G) is 0.19. This D/G ratio in SWCNT bundles usually indicates the presence of amorphous carbon[118].

Through the intensity of the RBM feature, the electronic type of the nanotubes can also be distinguished. Very close but intense RBM features are observed in the region from $\sim 150cm^{-1}$ to $\sim 350\ cm^{-1}$ as observed in Figure5.1a). The most intense peaks in the RBM region of the pristine spectrum are seen at around 244, 261 and $269cm^{-1}$. This RBM spectrum agrees with the peaks from a study performed on HiPco® bundles with a green laser (1.41 eV)[96]. The high number of frequencies observed in this region, corresponds to a diameter distribution of different SWCNTs in resonance at this excitation laser which suggest a large number of chiralities present in the pristine sample.

5.2 SWCNTs dispersion in THF
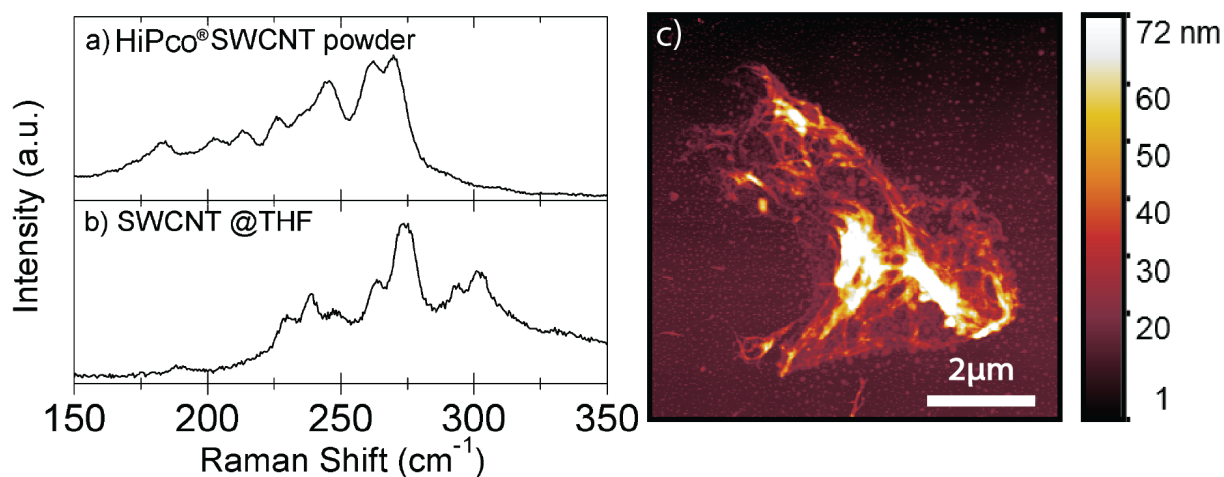
Figure 5.2: Raman spectrum (under 532 nm excitation) of a) RBM region of HiPco® SWCNT, b) RBM region of sonicated SWCNT in THF c)AFM image of sonicated SWCNT bundles in THF.

Before starting the separation process, the dispersion of the nanotubes in the organic solvent to be used, was tested by sonicating the pristine SWCNTs powder in THF during 5 min at a concentration of 1:10 $[mg/ml]$. Figure 5.2 show the Raman spectra at the RBM region (from $\sim 150cm^{-1}$ to $\sim 350\ cm^{-1}$) of a) pristine SWCNT powder with

respect to b) dispersed SWCNT in THF. The profile of the RBM region in the case of the pristine HiPco$^®$ SWCNTs has altered after dispersion. There is a significant decrease in the intensities of the lowest frequency peaks (from 175 to 220 cm^{-1}) meanwhile, the peaks present from 225 to 275 cm^{-1} are more distinguished. Two well separated peaks with RBM 295 and 305 cm^{-1} appear. These increment in intensity is due to a higher resolution of the resonant tubes which occurs when a greater freedom of vibration is allowed, indicating that the tubes are less bound together[119]. Further, the appearance and fading of peaks at higher and lower frequencies in the RBM region respectively suggest the enrichment towards a higher frequency resonant tubes. Figure 5.2 c) shows an AFM image of the pristine SWCNT dispersed in THF sample previously analyzed by Raman spectroscopy. The image shows a SWCNT bundle that starts to unravel. At the center of the bundle, nanotube entanglement is still present with a height up to 72 nm. From it the nanotubes spread out in smaller bundles which is observed mostly at the edges of the sample and agrees with the the Raman spectroscopy analysis of initial deblundling and a reduction of the bundle size of the nanotubes.

5.3   Intercalation of HiPco$^®$ SWCNTs
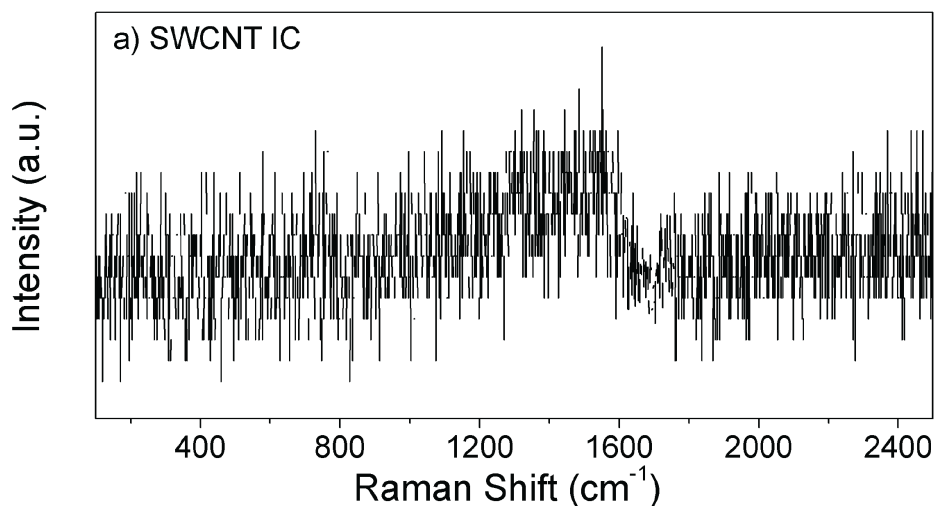
Figure 5.3: Raman spectrum of SWCNT intercalation compound taken with 532 nm laser thought an optical window.

Intercalations (KC_8, KC_{24} and NaC_8) were performed inside a globe box under an Ar atmosphere as previously described in Chapter 3. The corresponding amount of SWCNTs and potassium/sodium respectively were weighted and added in a glass vial and placed over a heating plate for 72 hours. After the melting of the potassium/sodium with the pristine powder of SWCNTs, the formation of SWCNT intercalation compound is verified *via* Raman spectroscopy. As previously explained in chapter 4, GIC are extremely sensitive to oxidation when exposed to ambient conditions. Therefore, to perform the Raman measurement, an optical window was implemented. The

sample was sealed inside the globebox by a two CF flanges system joined with a Cu ring wiht a glass window on one side. This technique permits an accurate Raman measurement by maintaining the sample under the same environmental conditions as inside the globe box. Raman spectroscopy has been a technique used as a tool for the analysis of GIC mechanisms[120]. The G-mode gets affected by the interaction of the atoms produced by charge transfer or doping[121]. According to Grimm[122], any type of added charge carrier (hole or electron) will reduce the phonon vibration screening, producing a blue-shift of the G-mode. This upshift is explained with the combination of non-adiabatic (dynamic) effects[123]. When doped, the shape of the G-mode gets modified by a coupling and the interference with the conduction electrons and phonons inducing a Fano line-shape around 1510 cm^{-1}[124]. Figure 5.3 shows a Raman spectrum of SWCNT intercalation compound measured inside an optical window with a 532 nm laser. The sample exhibits the characteristic broad Fano-line shape spectrum at $\sim$ 1540 cm^{-1} as reported in the literature[124,125] from which we can a certain successful intercalation of SWCNTs to be used for the separation.

5.4   SET I
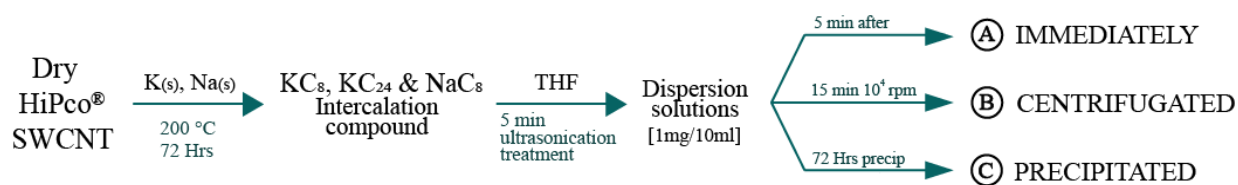
Figure 5.4: First batch of samples prepared using one sonication three samples prepared at different conditions of KC_8 KC_{24}, NaC_8

A scheme of the first set of processes implemented to achieve individualization of the SWCNTs (see Figure 5.4). Three samples were prepared, one for each intercalation compound: KC_8, KC_{24} and NaC_8 respectively. These samples were subjected to a dispersion in THF at a concentration of 1:10 [mg/ml] and then tip sonicated during 5 min. From this step of the separation process (after dispersion), samples were prepared under three different conditions. This corresponds to process A (immediately), B (centrifuged) and C (precipitated).

The first process from **SET I** (**process A**) was prepared by placing a drop from the supernatant onto a silicon wafer, 5 min after sonication process ended. The wafer was further dried inside a vacuum oven at 80°C and then analyzed by AFM microscopy. This characterization method provides information about the nanotubes/bundles length and an approximation of its height profile. In Figure 5.5 bundles of single-wall carbon nanotubes after the separation **process A**(immediately) can be observed in the AFM images for each intercalation compound sample. A qualitative analysis of the dispersion between the three different intercalation compounds observed at a)KC_8, c) KC_{24}, e)NaC_8 shows a bigger bundle size of KC_8, with a bundle height up to 500nm. It suggest a lower dispersion quality of KC_8 compared to KC_{24} and NaC_8. A close up of each AFM image, performed at the dashed square area, is observed in
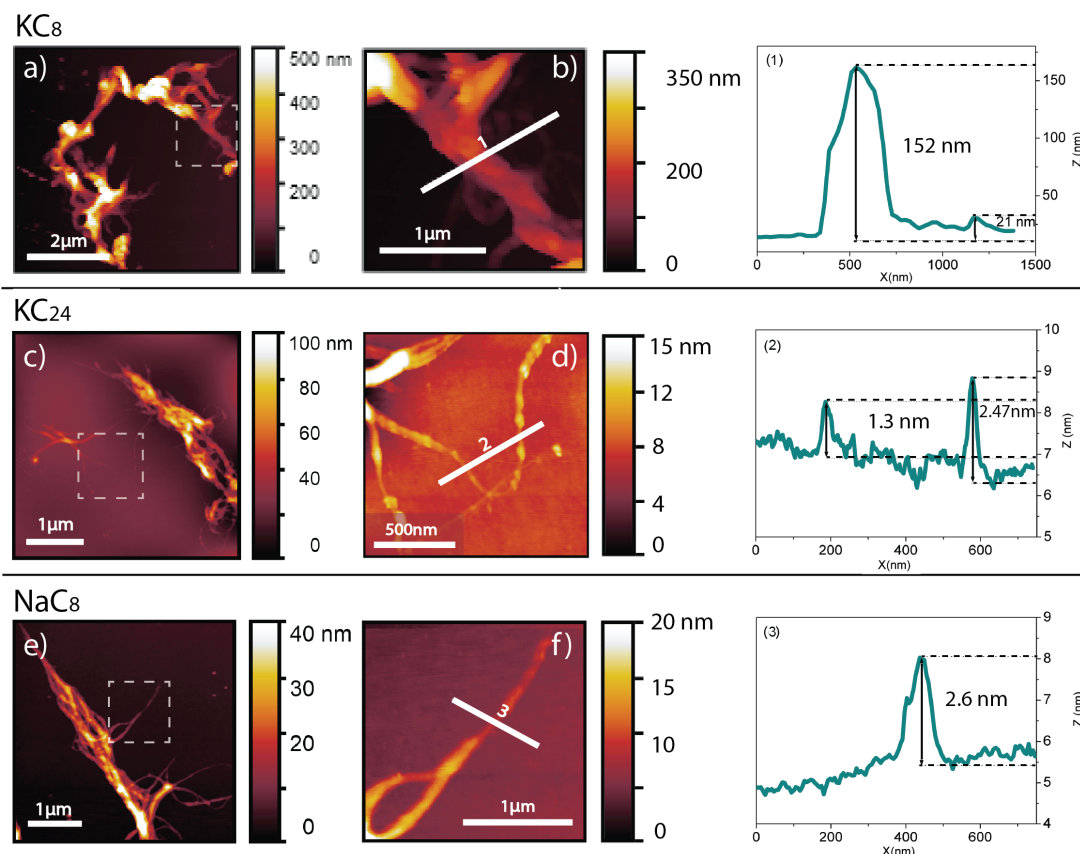
Figure 5.5: AFM image of bundles (left side) of a)KC_8, b)KC_{24}, c)NaC_8 samples from separation process A, stage I. Top view AFM image close up (left side) and height profile of SWCNT separated bundles 1,2,3 respectively.

b), d) and f). They corresponds to the smallest bundles observed along the samples. A height profile was performed along the thinnest fiber like bundles of each sample profiles 1, 2, 3 from KC_8, KC_{24} and NaC_8 respectively. The height profile shows a difference of one order in magnitude between the bundle height from KC_8 profile 1 (152 nm) compared to profile 2 and 3 KC_{24} (1.3 and 2.47 nm) and NaC_8 (2.6 nm) respectively. For this reason, KC_8 is discarded for subsequent separation processes.

From the previous separation **Process A**(immediately), the AFM images profiles, showed a decrease in size of the dispersed nanotubes bundles up to 1.3 nm but the dispersion along the sample was not uniform since the maximum height of the bundles from KC_8, KC_{24} and NaC_8 was 500, 100 and 40 nm respectively. Therefore the second separation process from **SET I** was performed in order to obtain a more homogeneous separation. **Process B**(centrifuged) consist in a 15 min centrifuging process at 10000 rpm after tip sonication dispersion for both samples:
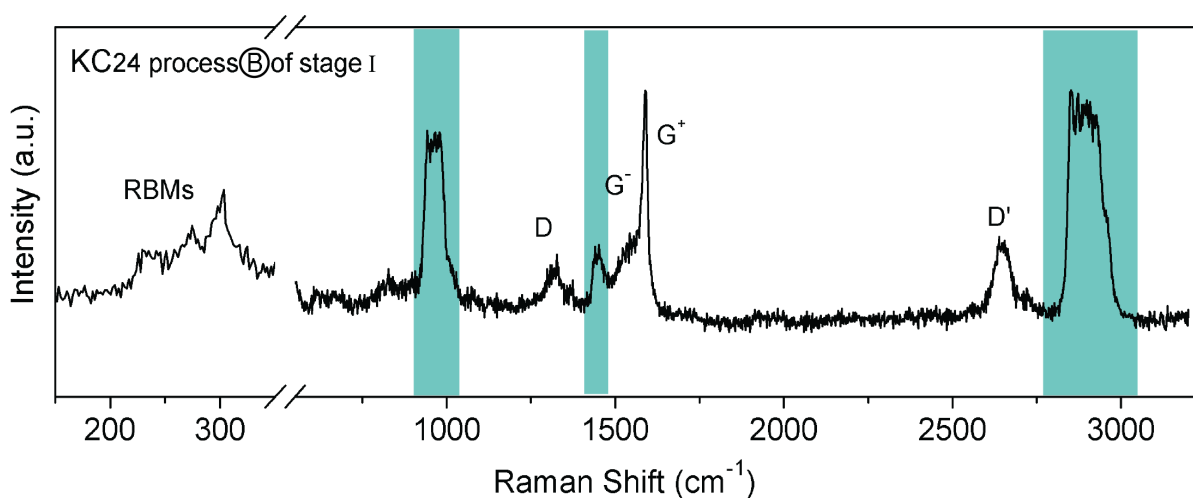
Figure 5.6: Raman spectrum of **process B**(centrifuged) of KC_{24} from **SET I**. Raman Spectrum show the four characteristic peaks of SWCNTs (RBM-mode, D-mode, G-mode and D'-mode) but there is also the presence of two additional peaks (blue shaded stripes) assigned to polypropylene contamination originated from the decomposition of plastic ware (eppendorfs) due to contact with THF.

KC_{24} and NaC_8. The Raman spectrum of the KC_{24} at this **Process B** is shown in Figure5.6. Despite the fact that the characteristic peaks from SWCNTs (RBM-mode, D-mode, G-mode and D'-mode) are present in the spectrum, the sample exhibits additional peaks located at near 3000 cm^{-1} and $\sim$ 1450 cm^{-1} as shown in the blue stripes in Figure5.6. The origin from this peaks, reveals the presence of polypropylene (PP)[126]. The spectral signature of PP can be attributed to plastic laboratory wave contamination obtained by decomposition of the eppendorfs in contact with THF. Consequently, **Process B** is neglected for further separations.

After **Process B** failed to obtain a better dispersion, another approach to achieve a homogeneous dispersion was performed. **Process C** consists in leaving the KC_{24} and NaC_8 samples resting for 72 hours after the dispersion process. Sitting time is done to allow heavier (bigger) bundles to precipitate and be able to reach smaller and more separated nanotubes. Then a drop from about 2/3 of height of the solution was taken from, and drop-casted into a SiO_2 wafer substrate with further dried inside a vacuum oven at 80°. Raman spectroscopy analysis was performed on both intercalation samples (KC_{24} and NaC_8) in the RBM region from 100 cm^{-1} to 350 cm^{-1} as observed in Figure5.7. The difference in intensity along the y-axis is arbitrary. The spectra shows the RBM Raman feature of KC_24 (blue line) and NaC_8 (black line) samples at **Process C** from **SET I**.

Compared to the pristine sample, both spectrum (KC_{24} and NaC_8) show a higher number of peaks along the RBM region 13 and 9 peaks respectively compared to the amount of peaks from both the pristine sample (7 peaks) observed in Figure5.1 a) and pristine SWCNT dispersed in THF without intercalation (7peaks) observed in Figure5.2
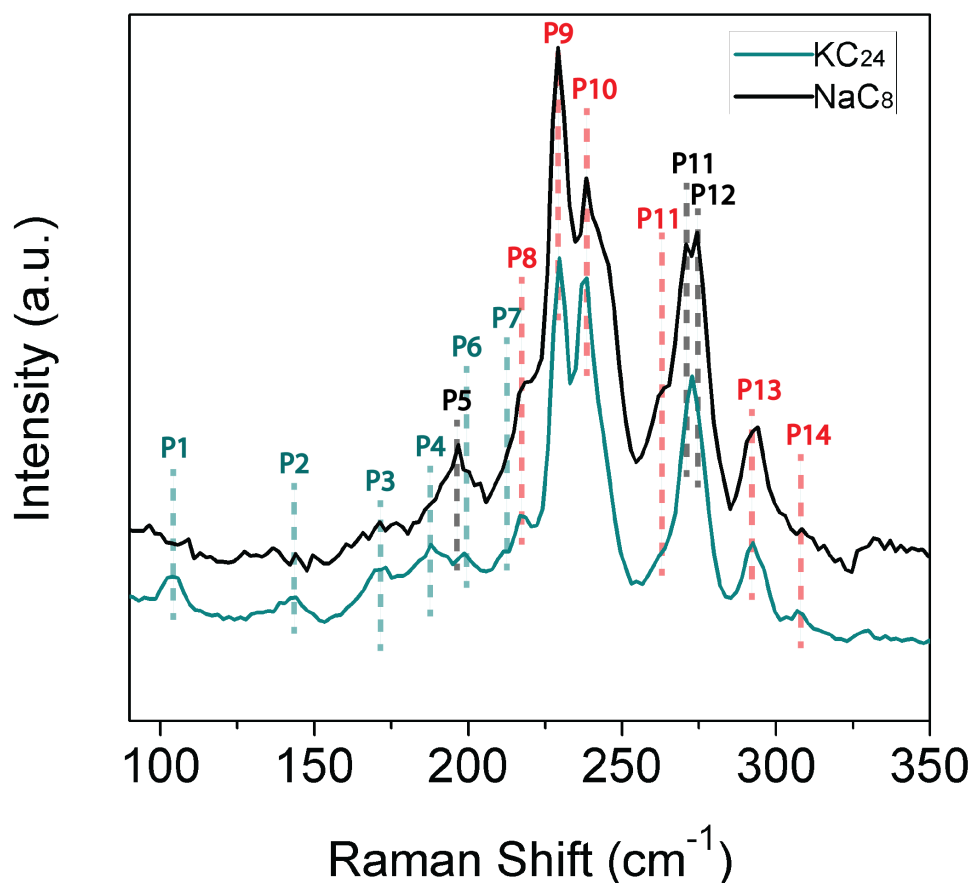
Figure 5.7: RBM Raman spectra of KC_{24} and NaC_8 at process C from the first batch. It presents peaks corresponding to RBMs frequencies resonant nanotubes at 532 nm laser.

b). In pristine spectrum shown in Figure 5.1, there is an intense double peak displayed at around 266 cm^{-1}, after the separation **Process C** is performed, this peak gets split into 2 and 3 peaks for potassium and sodium samples respectively. Each peak correspond to a carbon nanotube in resonance with the excitation energy laser[95]. A higher number of peaks present in the sample will relate directly with the debundling condition of the SWCNT. The RBM-feature is composed by a number of individual peaks in both samples (KC_{24} and NaC_8) at 217, 229, 239, 264, 293, 306 cm^{-1} positions identified as red dashed lines in the Figure5.10. Peaks P13 and P14 at the higher frequency region were not observed in the pristine sample. KC_{24} sample show high individualization in peaks P9 and P10 compared to NaC_8. The presence of peaks P1, P2, P3 and P4 in the KC_24 spectrum compared to the pristine spectrum were no peak is observed bellow 150 cm^{-1}, suggest a preferential separation towards lower frequency (bigger tube diameters)[117]. The results after the precipitation time implemented in this **Process C**, shows an improvement in the

separation process. This process will be used as a baseline for the next batch of samples prepared (**SET II**).

5.5 SET II
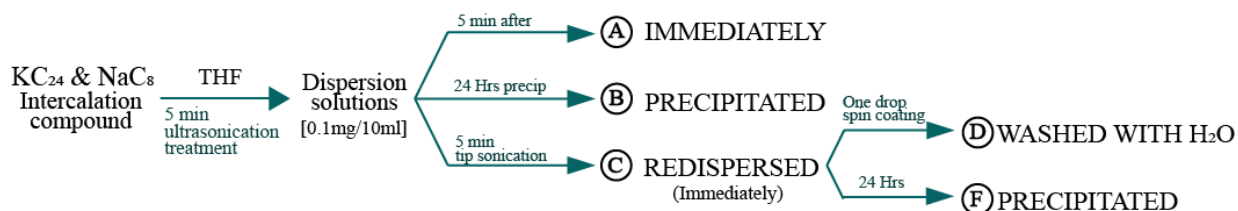
Figure 5.8: Second batch of samples prepared using a concentration of 1:10 $[0.1mg/1mL]$ three samples prepared at different conditions of KC_{24} and NaC_8.

The second set of processes was prepared with two intercalation samples KC_{24} and NaC_8 at a lower concentration of the intercalation compound with respect to the solvent (THF). 0.1 mg per 1 mL concentration was used to prepare 10 ml of each solution. Then samples were dispersed by tip sonication during 5min. Figure 5.8 shows a scheme of the procedure for the 5 dispersion processes of **SET II** under different sample preparation parameters corresponding to A(immediately), B(precipitated), C(redispersed). These three samples were prepared after the tip sonication dispersion. From the samples at process C, two subsequent processes were performed on them. D(washed with H_2O) and E(precipitated).

Process A(immediately) from **SET II** follows the same procedure as **process B** from **SET I**, the samples were dropcasted onto a SiO_2 5 min after the dispersion and further dried under the same conditions(vacuum oven at 80°C).Figure 5.9 show a AFM image of a)KC_{24} and b)NaC_8 at **process A**. A qualitative analysis of the AFM images from the bundles show a decrease in size and a cleaner sample which suggest dispersion is improved with respect to previous processes from **SET I**. The maximum bundle height from both potassium and sodium samples are around 192 and 107 nm respectively.

A height profile was performed in two places from the $KC24$ (see Figure 5.9 profile 1 and 2). The height profile shows a bundle height of 32 and 10.26 nm for profile 1 and 2 respectively. This value is bigger than the previous process separation process from **SET I**. The results obtained when the profiles from b) NaC_8 in Figure 5.9 are analyzed, show the same pattern. The bundles height from profile 3 and 4 are 56.77 and 6.72 nm respectively. Therefore, to obtain better results, samples were left at rest 24 hours and then a each sample was drop-casted onto SiO$_2$ wafer. This process is called **process B** from **SET II**.
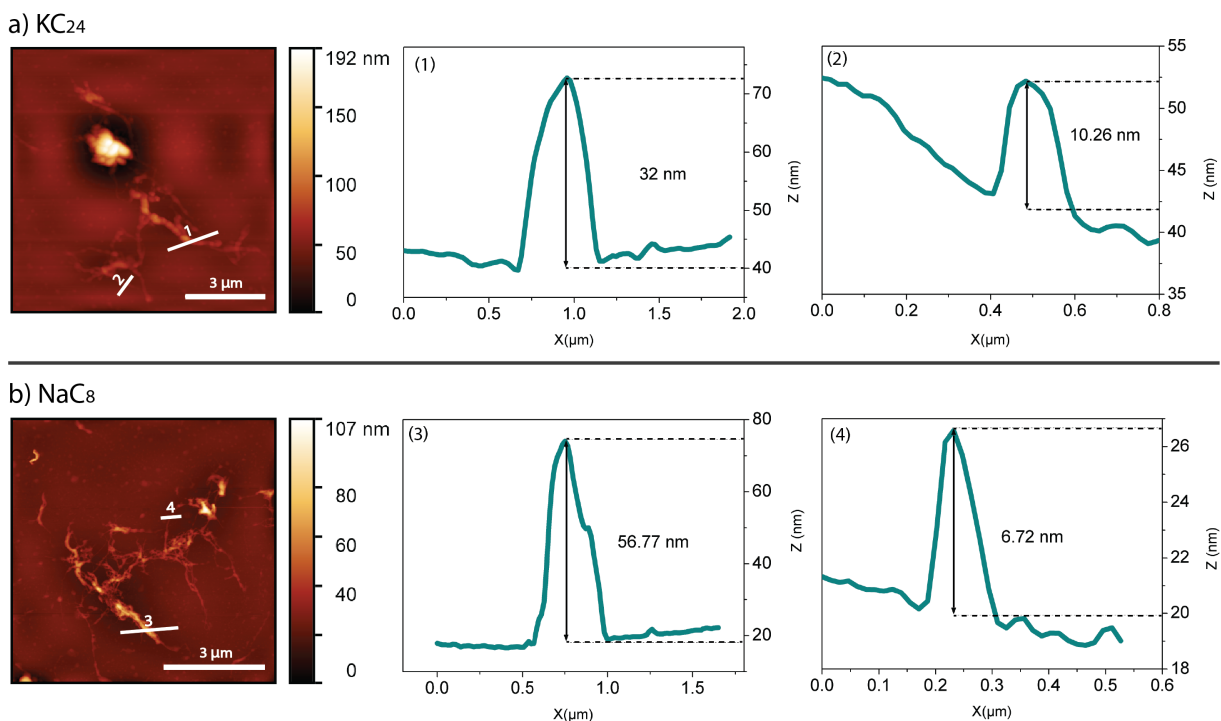
a) KC$_{24}$

b) NaC$_8$

Figure 5.9: AFM image of bundles of a)KC_{24}, b)NaC_8 samples from separation process A(immediately),**SET II**. a.1), a.2), b.3) and b.4) show a height profile AFM image height profile performed on the dispersed bundles along the samples along the white lines of SWCNT separated bundles 1,2,3,4.

The sample characterization of KC$_{24}$ and NaC$_8$ subjected to process B(precipitated) from **SET II** is presented in Figure 5.10 a) and b) respectively. As expected, AFM image of KC$_{24}$ (see Figure 5.10 a) show a significant decrease in the bundle size from about 200 nm to 15 nm. The same result applies to NaC$_8$ sample where the decrease in maximum bundle height goes from about 100 nm to 30 nm. A profile was performed on both samples showing the smallest bundles from the area analyzed at about 1.19nm with the smallest height at KC_{24} sample (see Figure 5.10 a.1) and 1.65nm at sodium profile (see Figure 5.10 b.2).

Despite the fact that there is a considerable decrease in the height of the profiles from the previous process analyzed (**B precipitated**), the width measured of the NaC_8 bundles show a difference of about 30 nm, twice the size of KC_{24} bundles. Hence, thus the sodium sample after 24 hour precipitation time was re-dispersed. From the 10 ml sample, 1/3 of the top part was extracted and transferred to a new glass vial and tip sonicated again for 5 min. Figure5.11 shows a Raman spectra of the NaC$_8$ sample from the previous **process B** (precipitated), **SET II** at two spots (see Figure 5.11 a) and b)) compared to the samples after the second tip sonication (**process C, redispersed**) at two different spots (see Figure 5.11 c) and d)). The two lower spectra show an intense peak at around 300 nm.
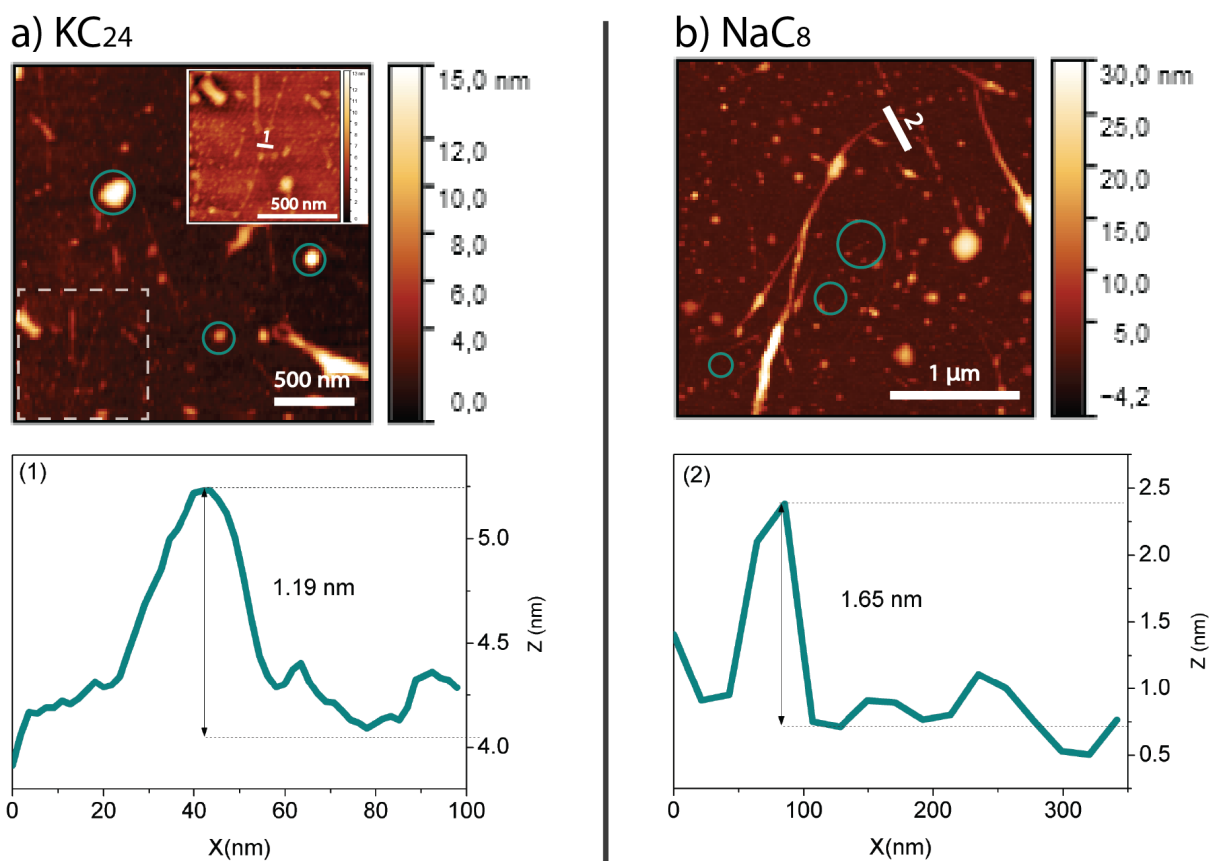
Figure 5.10: AFM image of a)KC_{24} and b)NaC_8 from separation **process B** (precipitated) from **SET II**. a.1) show a height profile from a fiber like structure from a close up of the $KC_2 4$ sample. b.1) show a lateral height profile of a small carbon nanotube bundle from NaC_8.

The appearance of a peak at a high frequency position can be attributed to the fact that nanotubes get charged upon intercalation which will make the tube show a metallic-like behavior[127].

Although this process shows a better separation, there is a lot of residue along the sample substrate as it can be observed circled in blue across the AFM in Figure5.10 a) and b). To attempt to clean and decrease the number of residues and functionalization of the samples, a new further process is implemented after the dispersion. Samples prepared and analyzed over SiO_2 in the **process C** were placed in the spin coating and washed down with to two drops of water and then dried inside a vacuum oven, this is referred as **process (D)** (washed with H_2O) from **SET II**. A small amount of water will act as residue removal. The sample of NaC_8 was analyzed through Raman spectroscopy in the same spots as in the previous process after the second dispersion. A comparative result of the spectra at these
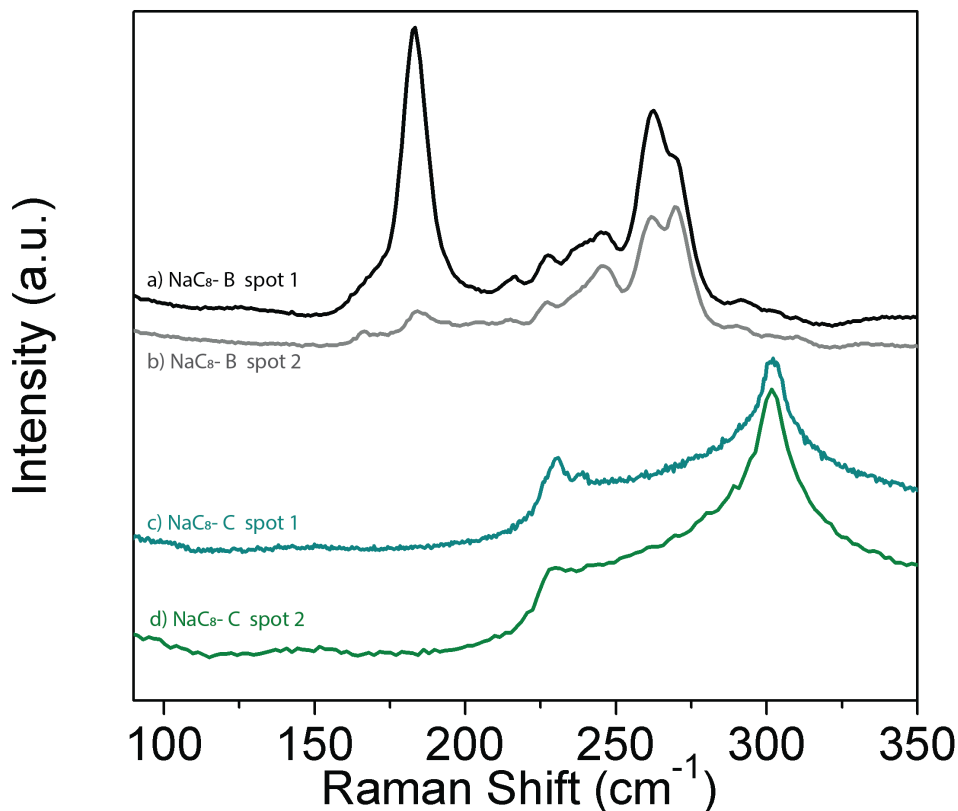
Figure 5.11: Raman spectra of NaC_8 after the second dispersion immediately (greenish spectra) vs NaC_8 from process (B) (grey spectra)

two processes is displayed in Figure 5.12 (the different spectra displayed in the figure are shifted along the y-axis to better observe them). The figure shows two different spots from the sample before and after the washing process. Figure5.12 a) exhibits an increase in the intensity of the peak from the D-mode observed in the red dashed circle. Recalling its relation to disorder, the increment in the D-mode can be attributed to a higher functionalization of the nanotubes. This spectra also shows the fading of some peaks in the RBM region. This is observed in Figure5.12 a) where two peaks (* and **) at 163 cm^{-1} and , 185 cm^{-1} vanishes after the **process D**. The fading of the same peak (*) is observed in the second spot analyzed (see Figure 5.12) b). Consequently this washing process wont be used for further separation processes. The difference in intensity between **process C** and **process D** was arbitrary assigned in order to better observe the difference in the peaks.

   Process E is the last process of the second batch (**SET II**). It was prepared after the second dispersion (**process C**), NaC_8 sample was left at rest for 24 hours and then a drop was drop-casted on a SiO_2. Fig5.13 a) show an
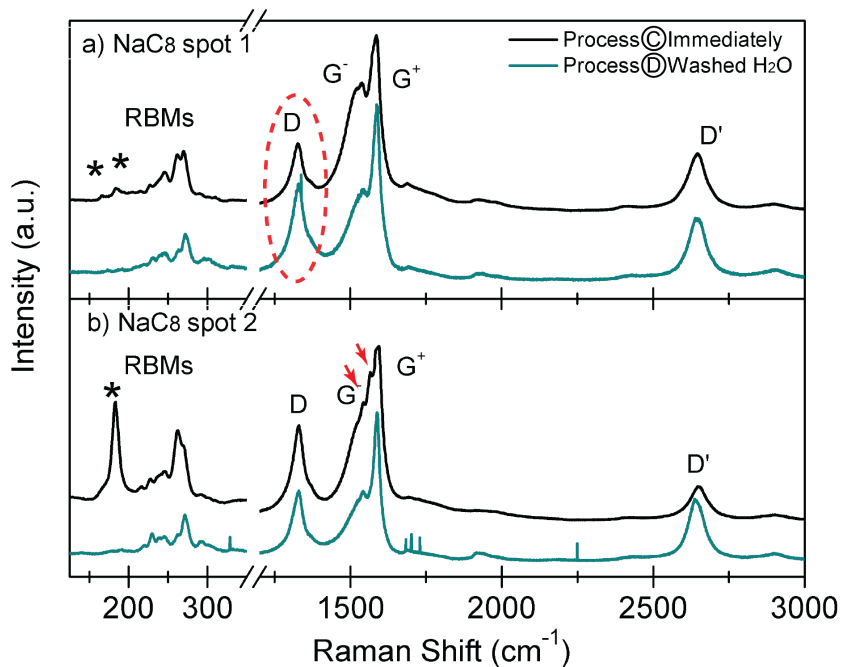
Figure 5.12: Raman spectra of NaC$_8$ sample from **process C**(redispersed) compared with **process D**(washed with H$_2$O)

AFM image of an area of 1.58 micro. This image show bundles up to 35 nm, but the entanglement of the nanotubes towards the end of the bundles show qualitative much smaller bundles. A close up image was performed in the sample along the dashed with square and is presented in Figure 5.13 b). A height profile was done on the thinnest stripe observed. The height of this bundle is 1.01 nm (see Figure 5.13 c)). The bundle size obtained from NaC_8 at **process E** now matches with the results from KC_{24} at the **process B**. By the end of this set of samples performed with a lower concentration, the parameters that affect the quality of the separation process can be identified. Then the third batch of samples was prepared (**SET III**) based on the best results from the previous processes.

5.6   SET III

Figure 5.14 shows a scheme of the process followed for the last set of samples. Sodium and potassium intercalation compounds NaC_8 and KC_{24}, respectively, were prepared by following same process stablished in the previous sets. 10 ml of THF dispersion was performed with 1:10 [mg/ml] followed by a tip sonication during 5 min, sedimentation time of 24 hours and then a second tip sonication was performed on one-third of the 10 ml volume (from the top
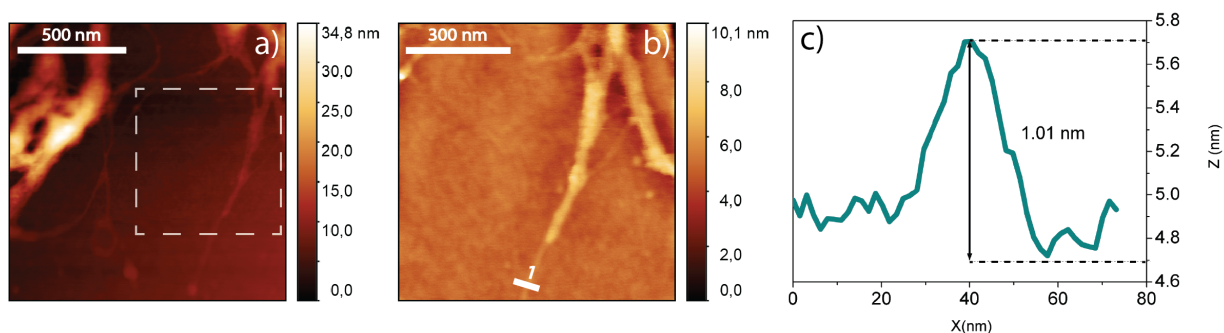
Figure 5.13: AFM images of NaC_8 at process (E) a) overview of the bundles, b) close up to a small strip 1) height profile of an individualized nanotube

part). At this part of the process, the first samples were prepared over a silicon dioxide substrate (**process A**) and the second set of samples were taken after 24-hour sedimentation (**process B**).
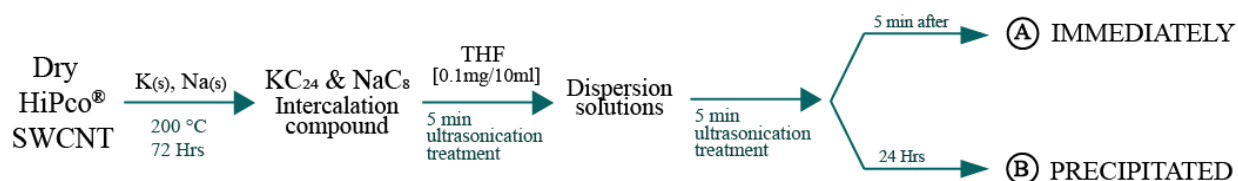
Figure 5.14: Third batch of samples prepared using a concentration of 1:10 [$0.1mg/1ml$] two sonications. Two samples prepared at different conditions of KC_{24}, NaC_8.

Figure5.15 show the analysis of the two processes from KC_{24} from **SET III** through Raman spectroscopy and AFM. Qualitative, AFM image from potassium sample immediately after the second sonication (see Figure 5.15 b)), shows a more homogeneous dispersion compared to previous samples were at the center of the nanotube bundle a higher bundle tangle was observed. Additionally, the presence of functionalization in the sample which is observed as particles of significant height along the substrate. A closer look is observed at part c) of Figure5.15. Residue particles are still present on the sample. A height profile along one fiber like structure, reveals a height of 1.17 nm, which is in the range of the diameter size from HiPco® SWCNTs samples (0.8-1.2 nm). After precipitation time, The amount of residue particles observed in the sample has decreased as seen in Figure5.15 e) and the image looks cleaner. A closer look into the sample is observed in Figure5.15 f) and it gives the height profile of a bundle of 1.66nm obtained by the profile 2 of the image. a Raman measurement was performed with a 532 nm laser in the RBM region between 150 and 350 cm^{-1} into KC_{24} sample for both processes (**A and B**) displayed as the gray dispersion in Figure5.15 a) and d) respectively.

a) KC24 (A) IMMEDIATELY

b) KC24 (B) PRECIPITATED
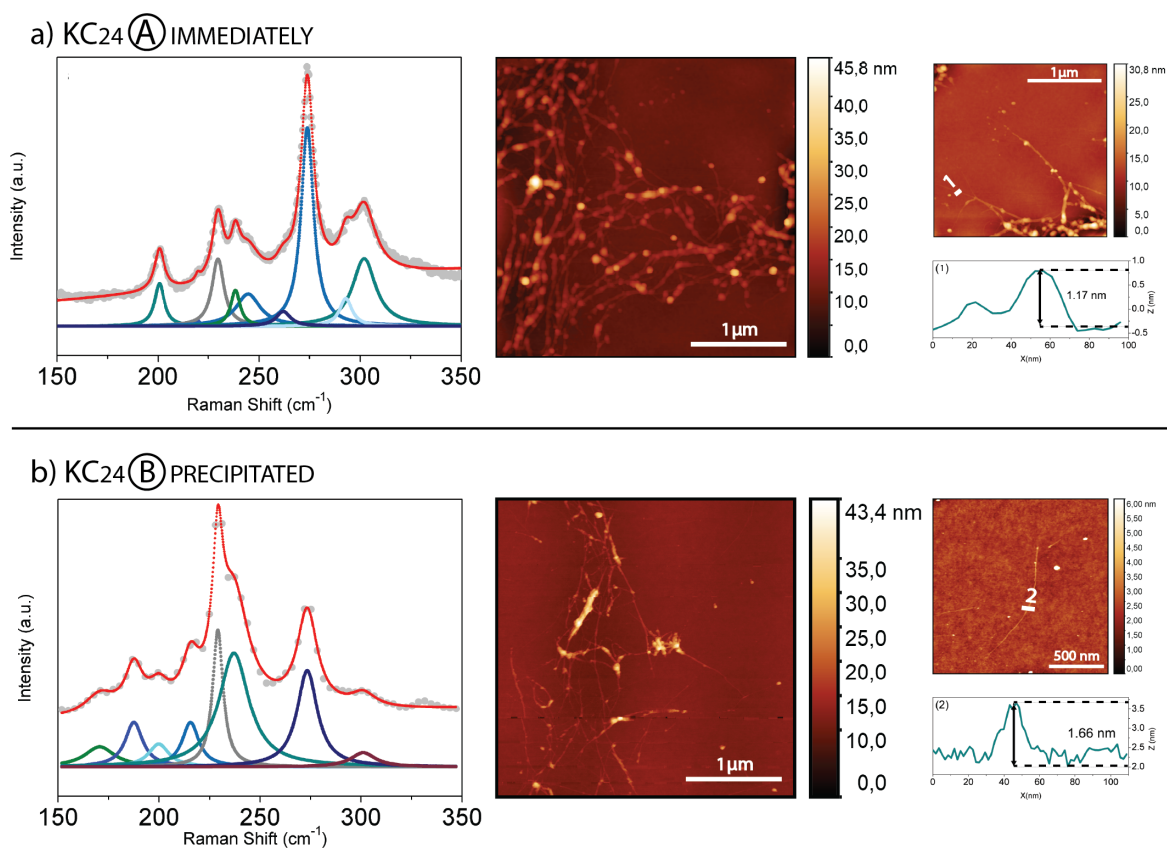
Figure 5.15: Characterization of KC_{24} from **SET III**. a) **process A** immediately and b)**process B**

A fitting was performed on both spectra to determine each peak in this region that corresponds to one chirality in resonance in the sample. The spectrum from potassium at **process A** can be fitted by 9 Gauss/Lorentz curves observed in red in Figure 5.15 a). It should be noted that no constraint of the line width has been applied in the fitting procedure. The fitted spectrum was profiled with the minimum number of features to avoid over interpretation. The most intense peak appears at 273.94 cm^{-1} followed by 4 medium intensity peaks at 200.7 cm^{-1}, 229.78 cm^{-1}, 238.41 cm^{-1}, 302.01 cm^{-1} and 4 small peaks at 219.78 cm^{-1}, 244.7 cm^{-1}, 262.04 cm^{-1}, 292.95 cm^{-1}. KC_{24} at **process B** Raman spectrum is observed in Figure 5.15 d). The fitted shapeline was obtained by 8 Gauss/Lorentz curves. The most intense peak is fitted by two peaks. The first located at 229.12 cm^{-1} with a small broadness and the second at 237.1 cm^{-1}. Two medium peaks are observed at 187.57 cm^{-1}, 273.35 cm^{-1} followed by four small peaks at 170.62 cm^{-1}, 199.85 cm^{-1}, 215.56 cm^{-1}, 301.05 cm^{-1}. By comparing the position of the two most intense peaks, a difference of the type (electronic) of nanotube that is resonant at that frequency can be observed; metallic for **process A** (immediately) an semiconducting for **process B**. The spectrum of the sample after precipitation time show a decrease in intensity of peaks at higher frequencies and the appearance of a higher number of peaks in lower

a) NaC8 (A) IMMEDIATELY

b) NaC8 (B) PRECIPITATED
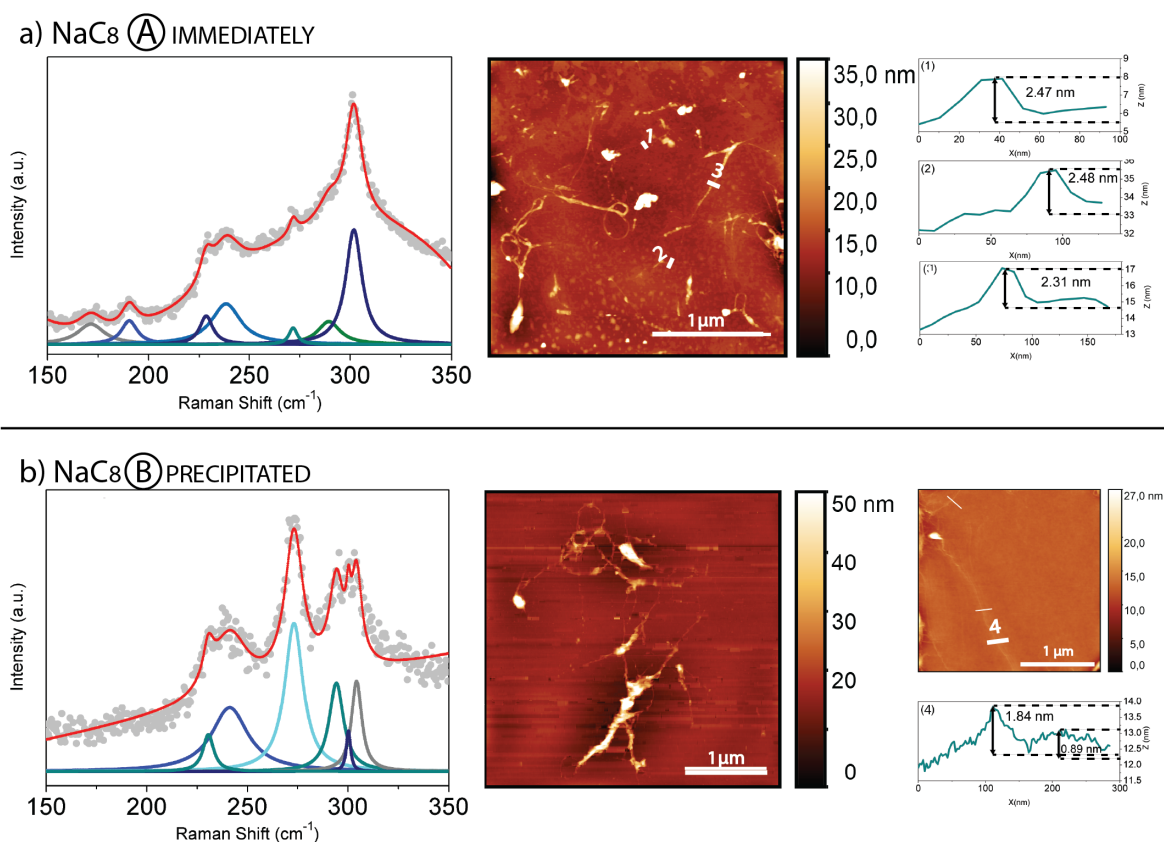
Figure 5.16: Raman spectrum of $KC_2 4$ at stage B (centrifuged) from stage I. It presents the characteristic peaks of SWCNTs but also shows characteristic peaks (blue shaded stripes) of polypropylene that originates from contamination from plastic ware when centrifuged.

frequencies ($150 cm^{-1}$ to $225 \ cm^{-1}$). This difference can be attributed to the fact that after precipitation time, some of the charge is loose and the nanotubes re-agglomerate. This is consistent with the profiles 1 and 2 from the AFM images where the size of the bundle after precipitation time is bigger.

Sodium samples were prepared under the same conditions as potassium (see Figure 5.14). AFM image from **process A** present a dispersion of the nanotubes bundles (See Figure5.16 b)). There are particles of about 35 nm height in the sample just as with potassium at the same process. Three AFM profiles were measured from the stripes along the substrate. They show a height of 2.47, 2.48 and 2.31 nm. After precipitation time, the amount of particles decrease just as with potassium samples.Figure 5.16 e) shows a nanotube bundle of the sodium sample at **process B**. A close up image of the AFM into one bundle in the precipitated process, shows an entanglement of the nanotubes

(see Figure 5.16 f). This is corroborate thought a height profile from (see Figure 5.16 f) that shows two bumps with a height of 1.84 and 0.89 nm. Raman characterization was performed on both samples with a 532 nm laser. The spectra from potassium for both **process A** and **process B** was fitted by 7 and 6 Gauss/Lorentz curves observed in Figure 5.16 a) and d) respectively. It is observed that the maximum peak located at agrees in frequency with the most intense peak from NaC_8 from **process C**(redispersed) from **SET II**. After the sample rested for 24 hours, it is observed that this peak gets split into three different peaks and the peaks from 150 to 200 cm^{-1}. The reduction in the number of peaks and the observed reduction in broadening of the peaks with respect to previous separation processes and the pristine material supports the conclusion of a debundle of the nanotubes has been achieved successfully. In the further section a chirality assignment of the the frequency of the fitted peaks is performed based on the concepts review in chapter 4.

5.6.1   Assignment of RBM frequencies

After determine the RBM frequencies from sodium and potassium at each process from **SET III**, we show in this section the assignment performed to a particular (n,m) chirality. The RBM frequency is proportional to the inverse diameter, $\omega_{RBM} = 1/d$[94]. But, recalling the additional coefficients A and B review in chapter 4, This coefficients will vary depending on several factors like the environment[95]. Therefore the equation that relates proportionally the frequency and the inverse diameter can not be used for the assignment.

A comparative analysis was performed with respect to literature of SWCNTs chiralities assignment studies. The work of Maultzsch,et al. about chiral index assignment[94], was used as reference to assign the chirality to each RBM frequency. Each frequency was compared to the experimental frequencies found in table 1 and 2 from her study[94] and the closest was assigned to its chirality (See table 1 column 1 show frequencies measured compared to the closest values from Maultzsch work are display in column 2). Each frequency peak was assigned to a particular chirality as shown in the table 1 were the chirality, diameter and electric type are displayed for all the four samples.

Additionally, the assignment was compared to three other references from the work of Strano[128] (REF 1), Fantini[129](REF 2) and Thomsen[116] (REF 3). The assignment of the nanotubes from these references differ in the sample description (use of surfactants of different dispersing agents). The assigned chiralities are presented in the last three columns of table 1. When compared the assigned chirality to the three additional references it is observed that there is a agreement in many of the assignment. Another interesting observation is the amount of metallic tubes assigned. For KC_{24} sample, a 66% of the tubes correspond to a metallic type in **process A** and 62% in **process B**. The same percentage is observed in sodium sample from **process A** (60%) meanwhile for **process B** the percentage is 50. This results suggest a preferential separation for metallic tubes.

⋮

	ωRBM(cm$_{-1}$)	ωRBM	Assigned chirality	d ref	S/M	Comparative assignment		
						REF 1	REF 2	REF 3
KC_{24}A	200.7	200.4	**(15,0)**	11.75	M	(15,0)	(15,0)	(14,2)
	219.78	220.3	**(13,1)**	10.60	M	(13,1)	(12,3)	(12,3)
	229.78	230.4	**(8,7)**	10.18	S	(8,7)	(9,6)	(8,7)
	238.41	236.4	**(12,1)**	9.82	S	(10,4)	(10,4)	(10,4)
	244.7	246.4	**(8,6)**	9.53	M	(11,2)	(12,0)	(8,6)
	262.04	262.7	**(8,5)**	8.90	M	(8,5)	(8,5)	(11,1)
	273.94	272.7	**(9,3)**	8.47	M	(9,3)	(9,3)	(9,3)
	292.95	291.4	**(10,0)**	7.83	S	(8,3)	(6,6)	(10,0)
	302.01	305.4	**(7,4)**	7.55	M	(7,4)	(7,4)	(8,7)
KC_{24} B	170.62	174.5	**(14,5)**	13.36	M	(10,10)	(13,7)	-
	187.57	189.4	**(12,6)**	12.44	M	(10,9)	(12,6)	(15,2)
	199.85	200.4	**(15,0)**	11.75	M	(12,5)	(15,0)	(14,2)
	215.56	216	**(9,7)**	10.88	S	(9,7)	(8,8)	(9,7)
	229.12	230.8	**(13,0)**	10.18	S	(13,0)	(9,6)	(9,6)
	237.1	236.4	**(12,1)**	9.82	S	(10,4)	(10,4)	(10,4)
	273.35	272.7	**(9,3)**	8.47	M	(9,3)	(9,3)	(9,3)
	301.05	305.4	**(7,4)**	7.55	M	(7,4)	(7,4)	(8,3)
NaC_8 A	190.15	189.4	**(12,6)**	12.44	M	(12,6)	(12,6)	(11,7)
	228.66	228.1	**(12,2)**	10.27	S	(8,7)	(9,6)	(9,6)
	238.57	236.4	**(12,1)**	9.82	S	(10,4)	(10,4)	(10,4)
	272.03	272.7	**(9,3)**	8.47	M	(9,3)	(9,3)	(9,3)
	301.84	305.4	**(7,4)**	7.55	M	(7,4)	(7,4)	(8,3)
NaC_8 B	230.62	230.4	**(8,7)**	10.18	S	(8,7)	(9,6)	(8,7)
	241.24	244.9	**(12,0)**	9.40	M	(9,5)	(11,2)	(9,5)
	273.19	272.7	**(9,3)**	8.47	M	(9,3)	(9,3)	(9,3)
	294.25	291.4	**(10,0)**	7.83	S	(8,3)	(6,6)	(10,0)
	300.23	297.5	**(8,3)**	7.72	S	(7,4)	-	(8,3)
	304.3	305.4	**(7,4)**	7.55	M	(9,1)	(7,4)	(9,1)

Chapter 6

Conclusions & Outlook

In this research project we observed the implementation of a new separation method to individualize SWCNT without the use of any surfactant. Potassium and sodium were used to perform the intercalation with the pristine SWCNT and THF, a polar solvent, was used as the solvent in this dispersion. Through the run of several test arranged into three sets of samples, bad processes were discard and the optimal procedure was determined. The conditions for this separation process are based on the intercalation of NaC_8 and KC_{24} under two 5 min sonication with a concentration of 1:10 [mg/ml]. A Fitting of the RBM region of the Raman spectra was performed at two stages of the process (A) immediately and (B) precipitated. AFM images provide the height of the dispersed nanotubes which support the conclusion of the presence of individual nanotubes in the sample. The dispersion of the potassium samples show a thinner bundle dispersion in compare with potassium but sodium samples present a smaller amount of peaks corresponding to the amount of chiralities present in the sample. Most of the assigned chiralities match with the references. The ones that did not match,can be considered as a bad assignment. This cases are observed when the frequencies show a high difference from the theoretical data or should not be present because that chirality is not resonant at the laser used to excite the nanotubes. This anomalies can be caused by several reasons like the interaction of the substrate with the nanotubes, remaining solvent present or charge remaining among the tubes. This charged tubes will produce a shift of the RBM frequency and therefore a miss assignment. Based on the results, it can be concluded that a successful preferential separation process has been obtained. Further studies needs to be conducted to improve the assignment of the RBMs such as a resonant Raman analysis n order to determine the transition energies and has an accurate value of A and B. As well, further experiments can be performed under a different solvent or intercalation metal. From this separation, dispersed samples can be subjected to a sorting procedure like gel chromatography in order to classify the nanotubes upon their chirality.

Bibliography

[1] Bockrath, M.; Cobden, D. H.; McEuen, P. L.; Chopra, N. G.; Zettl, A.; Thess, A.; Smalley, R. E. Single-electron transport in ropes of carbon nanotubes. *Science* **1997**, *275*, 1922–1925.

[2] Dyke, C. A.; Tour, J. M. Covalent functionalization of single-walled carbon nanotubes for materials applications. *The Journal of Physical Chemistry A* **2004**, *108*, 11151–11159.

[3] others,, *et al.* Crystalline ropes of metallic carbon nanotubes. *Science* **1996**, *273*, 483–487.

[4] FUCHS, J.-N.

[5] Dresselhaus, M.; Dresselhaus, G.; Sugihara, K.; Spain, I.; Goldberg, H. Springer series in materials science. *Graphite fibers and filaments* **1988**, *1*.

[6] G, D.; S, D.; Riichiro, S. *Physical Properties Of Carbon Nanotubes*; World Scientific Publishing Company, 1998.

[7] Goerbig, M. Electronic properties of graphene in a strong magnetic field. *Reviews of Modern Physics* **2011**, *83*, 1193.

[8] Zhu, Q.; Oganov, A. R.; Salvadó, M. A.; Pertierra, P.; Lyakhov, A. O. Denser than diamond: ab initio search for superdense carbon allotropes. *Physical Review B* **2011**, *83*, 193410.

[9] Hazen, R. M.; Downs, R. T.; Jones, A. P.; Kah, L. Carbon mineralogy and crystal chemistry. *Reviews in Mineralogy and Geochemistry* **2013**, *75*, 7–46.

[10] Hodge, S. A.; Bayazit, M. K.; Coleman, K. S.; Shaffer, M. S. Unweaving the rainbow: a review of the relationship between single-walled carbon nanotube molecular structures and their chemical reactivity. *Chemical Society Reviews* **2012**, *41*, 4409–4429.

[11] Kroto, H. W.; Heath, J. R.; O'Brien, S. C.; Curl, R. F.; Smalley, R. E. C60: Buckminsterfullerene. *Nature* **1985**, *318*, 162.

[12] Yadav, B.; Kumar, R. Structure, properties and applications of fullerenes. *International Journal of Nanotechnology and Applications* **2008**, *2*, 15–24.

[13] Iijima, S.; Ichihashi, T. Single-shell carbon nanotubes of 1-nm diameter. *nature* **1993**, *363*, 603.

[14] Iijima, S. Helical microtubules of graphitic carbon. *nature* **1991**, *354*, 56.

[15] Oganov, A. R.; Hemley, R. J.; Hazen, R. M.; Jones, A. P. Structure, bonding, and mineralogy of carbon at extreme conditions. *Reviews in Mineralogy and Geochemistry* **2013**, *75*, 47–77.

[16] Radushkevich, L.; Lukyanovich, V. á. O strukture ugleroda, obrazujucegosja pri termiceskom razlozenii okisi ugleroda na zeleznom kontakte. *Zurn Fisic Chim* **1952**, *26*, 88–95.

[17] Yu, M.-F.; Lourie, O.; Dyer, M. J.; Moloni, K.; Kelly, T. F.; Ruoff, R. S. Strength and breaking mechanism of multiwalled carbon nanotubes under tensile load. *Science* **2000**, *287*, 637–640.

[18] Coleman, J. N.; Khan, U.; Gun'ko, Y. K. Mechanical reinforcement of polymers using carbon nanotubes. *Advanced materials* **2006**, *18*, 689–706.

[19] Wei, B.; Vajtai, R.; Ajayan, P. Reliability and current carrying capacity of carbon nanotubes. *Applied Physics Letters* **2001**, *79*, 1172–1174.

[20] Kim, P. L. shi, A. Majumdar, PL McEuen. *Phys. Rev. Lett* **2001**, *87*, 215502.

[21] Che, J.; Cagin, T.; Goddard III, W. A. Thermal conductivity of carbon nanotubes. *Nanotechnology* **2000**, *11*, 65.

[22] Osman, M. A.; Srivastava, D. Temperature dependence of the thermal conductivity of single-wall carbon nanotubes. *Nanotechnology* **2001**, *12*, 21.

[23] Berber, S.; Kwon, Y.-K.; Tománek, D. Unusually high thermal conductivity of carbon nanotubes. *Physical review letters* **2000**, *84*, 4613.

[24] Journet, C.; Maser, W.; Bernier, P.; Loiseau, A.; de La Chapelle, M. L.; Lefrant, d. S.; Deniard, P.; Lee, R.; Fischer, J. Large-scale production of single-walled carbon nanotubes by the electric-arc technique. *Nature* **1997**, *388*, 756.

[25] Mintmire, J.; White, C. Electronic and structural properties of carbon nanotubes. *Carbon* **1995**, *33*, 893–902.

[26] Endo, M.; Iijima, S.; Dresselhaus, M. S.; Publishers, E. S. *Carbon nanotubes*, 1st ed.; Oxford ; Tarrytown, N.Y. : Pergamon, 1996; "Reprinted from Carbon, vol. 33, nos. 1,2,7,12"–T.p. verso.

[27] Saito, R.; Fujita, M.; Dresselhaus, G.; Dresselhaus, u. M. Electronic structure of chiral graphene tubules. *Applied physics letters* **1992**, *60*, 2204–2206.

[28] Noked, M.; Soffer, A.; Aurbach, D. The electrochemistry of activated carbonaceous materials: past, present, and future. *Journal of Solid State Electrochemistry* **2011**, *15*, 1563.

[29] Reich, S.; Thomsen, C.; Maultzsch, J. *Carbon nanotubes: basic concepts and physical properties*; John Wiley & Sons, 2008.

[30] Saito, R.; Fujita, M.; Dresselhaus, G.; Dresselhaus, M. S. Electronic structure of graphene tubules based on C 60. *Physical Review B* **1992**, *46*, 1804.

[31] Dresselhaus, M.; Dresselhaus, G.; Saito, R. Physics of carbon nanotubes. *Carbon* **1995**, *33*, 883–891.

[32] Jorio, A.; Dresselhaus, M.; Saito, R.; Dresselhaus, G. Raman spectroscopy in graphene related systems. 2011. *ed: John Wiley & Sons*

[33] Dresselhaus, M.; Eklund, P. Phonons in carbon nanotubes. *Advances in Physics* **2000**, *49*, 705–814.

[34] Ando, Y.; Iijima, S. Preparation of carbon nanotubes by arc-discharge evaporation. *Japanese Journal of Applied Physics Part 2 Letters* **1993**, *32*, L107–L107.

[35] Kim, K. S.; Cota-Sanchez, G.; Kingston, C. T.; Imris, M.; Simard, B.; Soucy, G. Large-scale production of single-walled carbon nanotubes by induction thermal plasma. *Journal of Physics D: Applied Physics* **2007**, *40*, 2375.

[36] Guo, T.; Nikolaev, P.; Thess, A.; Colbert, D. T.; Smalley, R. E. Catalytic growth of single-walled manotubes by laser vaporization. *Chemical physics letters* **1995**, *243*, 49–54.

[37] Kruusenberg, I.; Alexeyeva, N.; Tammeveski, K.; Kozlova, J.; Matisen, L.; Sammelselg, V.; Solla-Gullón, J.; Feliu, J. M. Effect of purification of carbon nanotubes on their electrocatalytic properties for oxygen reduction in acid solution. *Carbon* **2011**, *49*, 4031–4039.

[38] Harris, J. D.; Raffaelle, R. P.; Gennett, T.; Landi, B. J.; Hepp, A. F. Growth of multi-walled carbon nanotubes by injection CVD using cyclopentadienyliron dicarbonyl dimer and cyclooctatetraene iron tricarbonyl. *Materials Science and Engineering: B* **2005**, *116*, 369–374.

[39] others,, *et al.* Preferential growth of semiconducting single-walled carbon nanotubes by a plasma enhanced CVD method. *Nano Letters* **2004**, *4*, 317–321.

[40] Li, W.; Xie, S.; Qian, L.; Chang, B.; Zou, B.; Zhou, W.; Zhao, R.; Wang, G. Large-scale synthesis of aligned carbon nanotubes. *Science* **1996**, *274*, 1701–1703.

[41] Meyyappan, M.; Delzeit, L.; Cassell, A.; Hash, D. Carbon nanotube growth by PECVD: a review. *Plasma Sources Science and Technology* **2003**, *12*, 205.

[42] Chhowalla, M.; Teo, K.; Ducati, C.; Rupesinghe, N.; Amaratunga, G.; Ferrari, A.; Roy, D.; Robertson, J.; Milne, W. Growth process conditions of vertically aligned carbon nanotubes using plasma enhanced chemical vapor deposition. *Journal of applied physics* **2001**, *90*, 5308–5317.

[43] Ren, Z.; Huang, Z.; Xu, J.; Wang, J.; Bush, P.; Siegal, M.; Provencio, P. Synthesis of large arrays of well-aligned carbon nanotubes on glass. *Science* **1998**, *282*, 1105–1107.

[44] Nikolaev, P.; Bronikowski, M. J.; Bradley, R. K.; Rohmund, F.; Colbert, D. T.; Smith, K.; Smalley, R. E. Gas-phase catalytic growth of single-walled carbon nanotubes from carbon monoxide. *Chemical physics letters* **1999**, *313*, 91–97.

[45] Prasek, J.; Drbohlavova, J.; Chomoucka, J.; Hubalek, J.; Jasek, O.; Adam, V.; Kizek, R. Methods for carbon nanotubes synthesis. *Journal of Materials Chemistry* **2011**, *21*, 15872–15884.

[46] Dai, H. Carbon nanotubes: opportunities and challenges. *Surface Science* **2002**, *500*, 218–241.

[47] Niyogi, S.; Hamon, M.; Hu, H.; Zhao, B.; Bhowmik, P.; Sen, R.; Itkis, M.; Haddon, R. Chemistry of single-walled carbon nanotubes. *Accounts of Chemical Research* **2002**, *35*, 1105–1113.

[48] Komatsu, N.; Wang, F. A comprehensive review on separation methods and techniques for single-walled carbon nanotubes. *Materials* **2010**, *3*, 3818–3844.

[49] Tkalya, E. E.; Ghislandi, M.; de With, G.; Koning, C. E. The use of surfactants for dispersing carbon nanotubes and graphene to make conductive nanocomposites. *Current Opinion in Colloid & Interface Science* **2012**, *17*, 225–232.

[50] Sinar, A.; Azni, N.; Azizan, M.; Zainuddin, F.; Hazizan, M. A.; Shuhadah, S.; Sahrim, H. Treatment Method for dispersion OF carbon nanotubes: a review. 2015.

[51] Huang, Y. Y.; Terentjev, E. M. Dispersion of carbon nanotubes: mixing, sonication, stabilization, and composite properties. *Polymers* **2012**, *4*, 275–295.

[52] others,, *et al.* The present status and key problems of carbon nanotube based polymer composites. *Express Polymer Letters* **2007**, *1*, 253–273.

[53] Jogi, B. F.; Sawant, M.; Kulkarni, M.; Brahmankar, P. K. Dispersion and performance properties of carbon nanotubes (CNTs) based polymer composites: a review. *Journal of Encapsulation and Adsorption Sciences* **2012**, *2*, 69.

[54] Thostenson, E. T.; Ren, Z.; Chou, T.-W. Advances in the science and technology of carbon nanotubes and their composites: a review. *Composites science and technology* **2001**, *61*, 1899–1912.

[55] Ma, P.-C.; Siddiqui, N. A.; Marom, G.; Kim, J.-K. Dispersion and functionalization of carbon nanotubes for polymer-based nanocomposites: a review. *Composites Part A: Applied Science and Manufacturing* **2010**, *41*, 1345–1367.

[56] Vaisman, L.; Wagner, H. D.; Marom, G. The role of surfactants in dispersion of carbon nanotubes. *Advances in colloid and interface science* **2006**, *128*, 37–46.

[57] Garg, A.; Sinnott, S. B. Effect of chemical functionalization on the mechanical properties of carbon nanotubes. *Chemical Physics Letters* **1998**, *295*, 273–278.

[58] Bahr, J. L.; Yang, J.; Kosynkin, D. V.; Bronikowski, M. J.; Smalley, R. E.; Tour, J. M. Functionalization of carbon nanotubes by electrochemical reduction of aryl diazonium salts: a bucky paper electrode. *Journal of the American Chemical Society* **2001**, *123*, 6536–6542.

[59] Whittingha, S. M. *Intercalation chemistry*; Elsevier, 2012.

[60] Rouxel, J.; Trichet, L.; Chevalier, P.; Colombet, P.; Ghaloun, O. A. Preparation and structure of alkali metal intercalation compounds. *Journal of Solid State Chemistry* **1979**, *29*, 311–321.

[61] Dresselhaus, M.; Dresselhaus, G. Intercalation compounds of graphite. *Advances in Physics* **1981**, *30*, 139–326.

[62] Xu, J.; Dou, Y.; Wei, Z.; Ma, J.; Deng, Y.; Li, Y.; Liu, H.; Dou, S. Recent Progress in Graphite Intercalation Compounds for Rechargeable Metal (Li, Na, K, Al)-Ion Batteries. *Advanced Science* **2017**, *4*, 1700146.

[63] Sereni, J. G. R. Reference Module in Materials Science and Materials Engineering. **2016**,

[64] Lerf, A. Storylines in intercalation chemistry. *Dalton Transactions* **2014**, *43*, 10276–10291.

[65] Ausman, K. D.; Piner, R.; Lourie, O.; Ruoff, R. S.; Korobov, M. Organic solvent dispersions of single-walled carbon nanotubes: toward solutions of pristine nanotubes. *The Journal of Physical Chemistry B* **2000**, *104*, 8911–8915.

[66] Jiang, C.; Saha, A.; Martí, A. Carbon nanotubides: an alternative for dispersion, functionalization and composites fabrication. *Nanoscale* **2015**, *7*, 15037–15045.

[67] Novikov, Y. N.; Vol'pin, M. E. Lamellar compounds of graphite with alkali metals. *Russian Chemical Reviews* **1971**, *40*, 733.

[68] Michael, L. Standard Operating Procedure: Storage and Handling of Alakli Metals. 2016; `https://chemsafety.chem.oregonstate.edu/content/sop-alkali-metals`.

[69] Urben, P. G.; Pitt, M. J.; Young, J. A. Chemical Education Today-Book & Media Reviews-Bretherick's Handbook of Reactive Chemical Hazards. *Journal of Chemical Education* **2007**, *84*, 768–769.

[70] Shriver, D. F.; Drezdzon, M. A.; Drezdzon, M. A. *The manipulation of air-sensitive compounds*; John Wiley & Sons, 1986.

[71] Perrin, D.; Armarego, W.; Perrin, D. Purification of Laboratory Chemicals 4th Edition. 1996.

[72] Rutherford, S.; Do, D. Characterization of carbon molecular sieve 3A. *Langmuir* **2000**, *16*, 7245–7254.

[73] Nireesha, G.; Divya, L.; Sowmya, C.; Venkateshan, N.; Babu, M. N.; Lavakumar, V. Lyophilization/freeze drying-an review. *International journal of novel trends in pharmaceutical sciences* **2013**, *3*, 87–98.

[74] Girolami, G. S.; Rauchfuss, T. B.; Angelici, R. J. *Synthesis and technique in inorganic chemistry: a laboratory manual*; University Science Books, 1999.

[75] Kotz, J. C.; Treichel, P. M.; Townsend, J. *Chemistry and chemical reactivity*; Cengage Learning, 2012.

[76] Reinig, R. R.; Ellern, A.; Sadow, A. D. Heteroleptic Four-Coordinate Tris (oxazolinyl) borato Iron (II) Compounds. *Inorganic chemistry* **2019**,

[77] Jensen, W. B. Holleman-Wiberg's Inorganic Chemistry (edited by Wiberg, Nils). 2002.

[78] Cupolillo, A.; Giallombardo, C.; Papagno, L. Electronic properties of alkali–metal intercalated single walled carbon nanotubes. *Surface science* **2007**, *601*, 2828–2831.

[79] Duclaux, L. Review of the doping of carbon nanotubes (multiwalled and single-walled). *Carbon* **2002**, *40*, 1751–1764.

[80] Greenwood, N. N.; Earnshaw, A. *Chemistry of the Elements*; Elsevier, 2012.

[81] Smith, E.; Dent, G. *Modern Raman spectroscopy: a practical approach*; Wiley, 2013.

[82] Kuzmany, H. *Solid-state spectroscopy: an introduction*; Springer Science & Business Media, 2009.

[83] Meyer, C. 12 Carbon Nanotubes.

[84] Krishnan, R.; Shankar, R. Raman effect: History of the discovery. *Journal of Raman Spectroscopy* **1981**, *10*, 1–8.

[85] Hahn, D. W. Raman scattering theory. *Department of Mechanical and Aerospace Engineering, University of Florida* **2007**,

[86] Long, D. A. *The raman effect*; Wiley,, 2002.

[87] Dresselhaus, M. S.; Jorio, A.; Hofmann, M.; Dresselhaus, G.; Saito, R. Perspectives on carbon nanotubes and graphene Raman spectroscopy. *Nano letters* **2010**, *10*, 751–758.

[88] Kizil, R.; Irudayaraj, J. *Modern Techniques for Food Authentication*; Elsevier, 2018; pp 193–217.

[89] Costa, S.; Borowiak-Palen, E.; Kruszynska, M.; Bachmatiuk, A.; Kalenczuk, R. Characterization of carbon nanotubes by Raman spectroscopy. *Materials Science-Poland* **2008**, *26*, 433–441.

[90] Pimenta, M.; Marucci, A.; Empedocles, S.; Bawendi, M.; Hanlon, E.; Rao, A.; Eklund, P.; Smalley, R.; Dresselhaus, G.; Dresselhaus, M. Raman modes of metallic carbon nanotubes. *Physical Review B* **1998**, *58*, R16016.

[91] Dresselhaus, M.; Dresselhaus, G.; Jorio, A.; Souza Filho, A.; Saito, R. Raman spectroscopy on isolated single wall carbon nanotubes. *Carbon* **2002**, *40*, 2043–2061.

[92] Brown, S.; Jorio, A.; Corio, a. P.; Dresselhaus, M.; Dresselhaus, G.; Saito, R.; Kneipp, K. Origin of the Breit-Wigner-Fano lineshape of the tangential G-band feature of metallic carbon nanotubes. *Physical Review B* **2001**, *63*, 155414.

[93] Kataura, H.; Kumazawa, Y.; Maniwa, Y.; Umezu, I.; Suzuki, S.; Ohtsuka, Y.; Achiba, Y. Optical properties of single-wall carbon nanotubes. *Synthetic metals* **1999**, *103*, 2555–2558.

[94] Maultzsch, J.; Telg, H.; Reich, S.; Thomsen, C. Radial breathing mode of single-walled carbon nanotubes: Optical transition energies and chiral-index assignment. *Physical Review B* **2005**, *72*, 205438.

[95] Cheng, Q.; Debnath, S.; Gregan, E.; Byrne, H. J. Vibrational mode assignments for bundled single-wall carbon nanotubes using Raman spectroscopy at different excitation energies. *Applied Physics A* **2011**, *102*, 309–317.

[96] Kukovecz, A.; Kramberger, C.; Georgakilas, V.; Prato, M.; Kuzmany, H. A detailed Raman study on thin single-wall carbon nanotubes prepared by the HiPCO process. *The European Physical Journal B-Condensed Matter and Complex Systems* **2002**, *28*, 223–230.

[97] Völkl, E. *Proceedings: Microscopy and Microanalysis 2002*; Cambridge University Press, 2002; Vol. 8.

[98] Goldstein, J. I.; Newbury, D. E.; Michael, J. R.; Ritchie, N. W.; Scott, J. H. J.; Joy, D. C. *Scanning electron microscopy and X-ray microanalysis*; Springer, 2017.

[99] Reimer, L. *Scanning electron microscopy: physics of image formation and microanalysis*; Springer, 2013; Vol. 45.

[100] others,, *et al. Scanning electron microscopy, X-ray microanalysis, and analytical electron microscopy: a laboratory workbook*; Springer Science & Business Media, 2012.

[101] Seiler, H. Secondary electron emission in the scanning electron microscope. *Journal of Applied Physics* **1983**, *54*, R1–R18.

[102] Duncumb, P.; Shields, P. The electron microprobe. *New York* **1966**, *7*, 490.

[103] Everhart, T. E.; Thornley, R. Wide-band detector for micro-microampere low-energy electron currents. *Journal of scientific instruments* **1960**, *37*, 246.

[104] Marinello, F. Atomic force microscopy in nanometrology: modeling and enhancement of the instrument. **2007**,

[105] Sarid, D. *Scanning force microscopy: with applications to electric, magnetic, and atomic forces*; Oxford University Press on Demand, 1994; Vol. 5.

[106] Howland, R.; Benatar, L. A practical guide to Scanning Probe Microscopy, Park Scientific Instruments, Sunnyvale, 1996. **1996**,

[107] Binnig, G.; Rohrer, H.; Gerber, C.; Weibel, E. Surface studies by scanning tunneling microscopy. *Physical review letters* **1982**, *49*, 57.

[108] Binnig, G.; Quate, C. F.; Gerber, C. Atomic force microscope. *Physical review letters* **1986**, *56*, 930.

[109] Zhong, Q.; Inniss, D.; Kjoller, K.; Elings, V. Fractured polymer/silica fiber surface studied by tapping mode atomic force microscopy. *Surface Science Letters* **1993**, *290*, L688–L692.

[110] Meyer, E. Atomic force microscopy. *Progress in surface science* **1992**, *41*, 3–49.

[111] Rabe, U.; Kester, E.; Scherer, V.; Arnold, W. *Acoustical Imaging*; Springer, 2002; pp 179–186.

[112] Scherer, V.; Arnold, W.; Bhushan, B. Lateral force microscopy using acoustic friction force microscopy. *Surface and Interface Analysis: An International Journal devoted to the development and application of techniques for the analysis of surfaces, interfaces and thin films* **1999**, *27*, 578–587.

[113] Drobek, T.; Stark, R. W.; Heckl, W. M. Determination of shear stiffness based on thermal noise analysis in atomic force microscopy: passive overtone microscopy. *Physical Review B* **2001**, *64*, 045401.

[114] Bonnell, D. Scanning probe microscopy and spectroscopy. *Theory, Techniques, and Applications* **2000**, *289*.

[115] Winkler, R.; Spatz, J.; Sheiko, S.; Möller, M.; Reineker, P.; Marti, O. Imaging material properties by resonant tapping-force microscopy: a model investigation. *Physical Review B* **1996**, *54*, 8908.

[116] Thomsen, C.; Reich, S. *Light Scattering in Solid IX*; Springer, 2006; pp 115–234.

[117] Dresselhaus, M. S.; Dresselhaus, G.; Saito, R.; Jorio, A. Raman spectroscopy of carbon nanotubes. *Physics reports* **2005**, *409*, 47–99.

[118] Ferrari, A. C.; Robertson, J. Raman spectroscopy of amorphous, nanostructured, diamond–like carbon, and nanodiamond. *Philosophical Transactions of the Royal Society of London. Series A: Mathematical, Physical and Engineering Sciences* **2004**, *362*, 2477–2512.

[119] Gregan, E.; Keogh, S.; Hedderman, T.; Chambers, G.; Byrne, H. J. Use of Raman spectroscopy in the investigation of debundling of single walled carbon nanotubes. 2005.

[120] Saitta, A. M.; Lazzeri, M.; Calandra, M.; Mauri, F. Giant nonadiabatic effects in layer metals: Raman spectra of intercalated graphite explained. *Physical review letters* **2008**, *100*, 226401.

[121] Tristant, D.; Wang, Y.; Gerber, I.; Monthioux, M.; Pénicaud, A.; Puech, P. Optical signatures of bulk and solutions of KC8 and KC24. *Journal of Applied Physics* **2015**, *118*, 044304.

[122] Grimm, S.; Schießl, S. P.; Zakharko, Y.; Rother, M.; Brohmann, M.; Zaumseil, J. Doping-dependent G-mode shifts of small diameter semiconducting single-walled carbon nanotubes. *Carbon* **2017**, *118*, 261–267.

[123] Das, A.; Sood, A. Renormalization of the phonon spectrum in semiconducting single-walled carbon nanotubes studied by Raman spectroscopy. *Physical Review B* **2009**, *79*, 235429.

[124] Chacón-Torres, J. C.; Wirtz, L.; Pichler, T. Raman spectroscopy of graphite intercalation compounds: Charge transfer, strain, and electron–phonon coupling in graphene layers. *physica status solidi (b)* **2014**, *251*, 2337–2355.

[125] Vecera, P.; Holzwarth, J.; Edelthalhammer, K. F.; Mundloch, U.; Peterlik, H.; Hauke, F.; Hirsch, A. Solvent-driven electron trapping and mass transport in reduced graphites to access perfect graphene. *Nature communications* **2016**, *7*, 12411.

[126] Socrates, G. *Infrared and Raman characteristic group frequencies: tables and charts*; John Wiley & Sons, 2004.

[127] Gebhardt, J.; Bosch, S.; Hof, F.; Hauke, F.; Hirsch, A.; Görling, A. Selective reduction of SWCNTs–concepts and insights. *Journal of Materials Chemistry C* **2017**, *5*, 3937–3947.

[128] Strano, M. S.; Doorn, S. K.; Haroz, E. H.; Kittrell, C.; Hauge, R. H.; Smalley, R. E. Assignment of (n, m) Raman and optical features of metallic single-walled carbon nanotubes. *Nano Letters* **2003**, *3*, 1091–1096.

[129] Fantini, C.; Jorio, A.; Souza, M.; Strano, M.; Dresselhaus, M.; Pimenta, M. Optical transition energies for carbon nanotubes from resonant Raman spectroscopy: Environment and temperature effects. *Physical review letters* **2004**, *93*, 147406.